GEROS-ISS: GNSS REflectometry, Radio Occultation and Scatterometry onboard the International Space Station

Wickert, Jens; Cardellach, Estel; Bandeiras, Jorge; Bertino, Laurent; Andersen, Ole Baltazar; Camps, Adriano; Catarino, Nuno; Chapron, Bertrand; Fabra, Fran; Floury, Nicolas; Høeg, Per

Published in:
I E E E Journal of Selected Topics in Applied Earth Observations and Remote Sensing

Link to article, DOI:
10.1109/JSTARS.2016.2614428

Publication date:
2016

Document Version
Publisher's PDF, also known as Version of record

Citation (APA):
Wickert, J., Cardellach, E., Bandeiras, J., Bertino, L., Andersen, O. B., Camps, A., ... Høeg, P. (2016). GEROS-ISS: GNSS REflectometry, Radio Occultation and Scatterometry onboard the International Space Station. I E E E Journal of Selected Topics in Applied Earth Observations and Remote Sensing, 9(10), 4552-4581. DOI: 10.1109/JSTARS.2016.2614428

GEROS-ISS: GNSS REflectometry, Radio Occultation, and Scatterometry Onboard the International Space Station

Jens Wickert, Estel Cardellach, *Member, IEEE*, Manuel Martín-Neira, *Senior Member, IEEE*, Jorge Bandeiras, Laurent Bertino, Ole Baltazar Andersen, Adriano Camps, *Fellow, IEEE*, Nuno Catarino, Bertrand Chapron, Fran Fabra, Nicolas Floury, Giuseppe Foti, Christine Gommenginger, Jason Hatton, Per Høeg, Adrian Jäggi, Michael Kern, Tong Lee, Zhijin Li, Hyuk Park, Nazzareno Pierdicca, *Senior Member, IEEE*, Gerhard Ressler, Antonio Rius, Josep Roselló, Jan Saynisch, François Soulat, C. K. Shum, Maximilian Semmling, Ana Sousa, Jiping Xie, and Cinzia Zuffada

***Abstract*—GEROS-ISS stands for GNSS REflectometry, radio occultation, and scatterometry onboard the International Space Station (ISS). It is a scientific experiment, successfully proposed to the European Space Agency in 2011. The experiment as the name indicates will be conducted on the ISS. The main focus of GEROS-ISS is the dedicated use of signals from the currently available Global Navigation Satellite Systems (GNSS) in L-band for remote sensing of the Earth with a focus to study climate change. Prime mission objectives are the determination of the altimetric sea surface height of the oceans and of the ocean surface mean square slope, which is related to sea roughness and wind speed. These geophysical parameters are derived using reflected GNSS signals (GNSS reflectometry, GNSS-R). Secondary mission goals include atmosphere/ionosphere sounding using refracted GNSS signals (radio occultation, GNSS-RO) and remote sensing of land surfaces using GNSS-R. The GEROS-ISS mission objectives and its design, the current status, and ongoing activities are reviewed and selected scientific and technical results of the GEROS-ISS preparation phase are described.**

***Index Terms*—Global Navigation Satellite Systems (GNSS) reflectometry, GNSS radio occultation, international space station, mean sea level, mesoscale ocean currents.**

I. INTRODUCTION

THE European Space Agency (ESA) Directorate of Human Space Flight and Operations released an announcement of opportunity in July 2011 in coordination with the Directorate of Earth Observation Programmes soliciting scientific experiments for the International Space Station (ISS) relevant to global climate change studies. Twenty-five letters of intent were received from 237 science team members. After a peer-review of the 16 received proposals and a scientific and technical evaluation, the GEROS-ISS (GEROS hereafter) proposal [1] was recommended to proceed to Phase A feasibility studies. The proposing GEROS team consisted of 12 scientists and engineers from four European countries (Germany, Denmark, Spain, Switzerland) and one scientist from U.S.

GEROS is a new and innovative ISS experiment primarily focused on exploiting reflected signals of opportunity from the GNSS satellites at L-band to measure key parameters of ocean surfaces which are relevant to characterize climate change. Secondary mission goals include global atmosphere and ionosphere observations using the GNSS radio occultation

---

Manuscript received April 28, 2016; revised August 30, 2016; accepted September 24, 2016. Date of current version October 14, 2016. This work was supported in part by ESA for the GARCA study under Contract C111952 and the Phase A industrial studies under Contracts 4000112188 and 4000112189, in part by ESA for the SPIR and flight campaign under Contract 4200022592, and in part by the Spanish Ministry of Economy and Competitiveness under Grant ESP2015-70014-C2-1-R and Grant ESP2015-70014-C2-2-R. The Ohio State University component of the research was supported by NASA under Grant NNX15AU99G. *(Corresponding author: Jens Wickert.)*

J. Wickert, M. Semmling, and J. Saynisch are with the German Research Centre for Geosciences GFZ, Potsdam 14473, Germany (e-mail: wickert@gfz-potsdam.de; maxsem@gfz-potsdam.de; saynisch@gfz-potsdam.de).

E. Cardellach, F. Fabra, and A. Rius are with the Institute of Space Studies of Catalonia/Institute of Space Sciences-Spanish National Research Council, Barcelona 08034, Spain (e-mail: estel@ice.cat; fabra@ieec.cat; rius@ieec.uab.es).

O. B. Andersen and P. Høeg are with the Technical University of Denmark, Kgs. Lyngby 2800, Denmark (e-mail: hoeg@space.dtu.dk).

J. Bandeiras, N. Catarino, and A. Sousa are with the DEIMOS Engenharia S.A., Lisboa 1998-023, Portugal (e-mail: jorge.bandeiras@deimos.com.pt; nuno.catarino@deimos.com.pt; ana.sousa@deimos.com.pt).

L. Bertino and J. Xie are with the Nansen Environmental and Remote Sensing Center, Bergen 5006, Norway (e-mail: laurent.bertino@nersc.no; jiping.xie@nersc.no).

A. Camps and H. Park are with the Universitat Politecnica de Catalunya, Barcelona 08034, Spain, and also with the Institute of Space Studies of Catalonia/CTE-UPC, Center for Space Technologies, Barcelona 08034, Spain (e-mail: camps@tsc.upc.edu; park.hyuk@tsc.upc.edu).

B. Chapron is with the Institut français de recherche pour l'exploitation de la mer, IFREMER—Centre de Brest, Pointe du diable, BP 70, 29280 Plouzane, France (e-mail: bertrand.chapron@ifremer.fr).

C. Gommenginger and G. Foti are with the National Oceanography Center, Southampton SO14 3ZH, U.K. (e-mail: cg1@noc.ac.uk; g.foti@noc.ac.uk).

N. Floury, J. Hatton, M. Kern, M. Martin-Neira, G. Ressler, and J. Roselló are with the European Space Agency, ESTEC, Keplerlaan 1, PO Box 299, NL-2200 AG Noordwijk, The Netherlands (e-mail: nicolas.floury@esa.int; jason.hatton@esa.int; michael.kern@esa.int; gerhard.ressler@esa.int; josep.rosello@esa.int).

A. Jäggi is with the University of Bern, Bern 3012, Switzerland (e-mail: adrian.jaeggi@aiub.unibe.ch).

F. Soulat is with the Space Oceanography Division, Collecte Localisation Satellites (CLS), 8-10 rue Hermès, 31520 Ramonville St-Agne, France (e-mail: fsoulat@cls.fr).

T. Lee, Z. Li, and C. Zuffada are with the Jet Propulsion Laboratory, California Institute of Technology, Pasadena, CA 91109 USA (e-mail: tlee@jpl.nasa.gov; zhijin@jpl.nasa.gov; cinzia.zuffada@jpl.nasa.gov).

N. Pierdicca is with the Sapienza University of Rome, Rome 00185, Italy (e-mail: nazzareno.pierdicca@uniroma1.it).

C. K. Shum is with the Ohio State University, Columbus, OH 43210 USA, and also with the State Key Laboratory of Geodesy and Earth's Dynamics, Institute of Geology and Geophysics, CAS, Wuhan 430077, China (e-mail: ckshum@osu.edu).

Color versions of one or more of the figures in this paper are available online at http://ieeexplore.ieee.org.

Digital Object Identifier 10.1109/JSTARS.2016.2614428

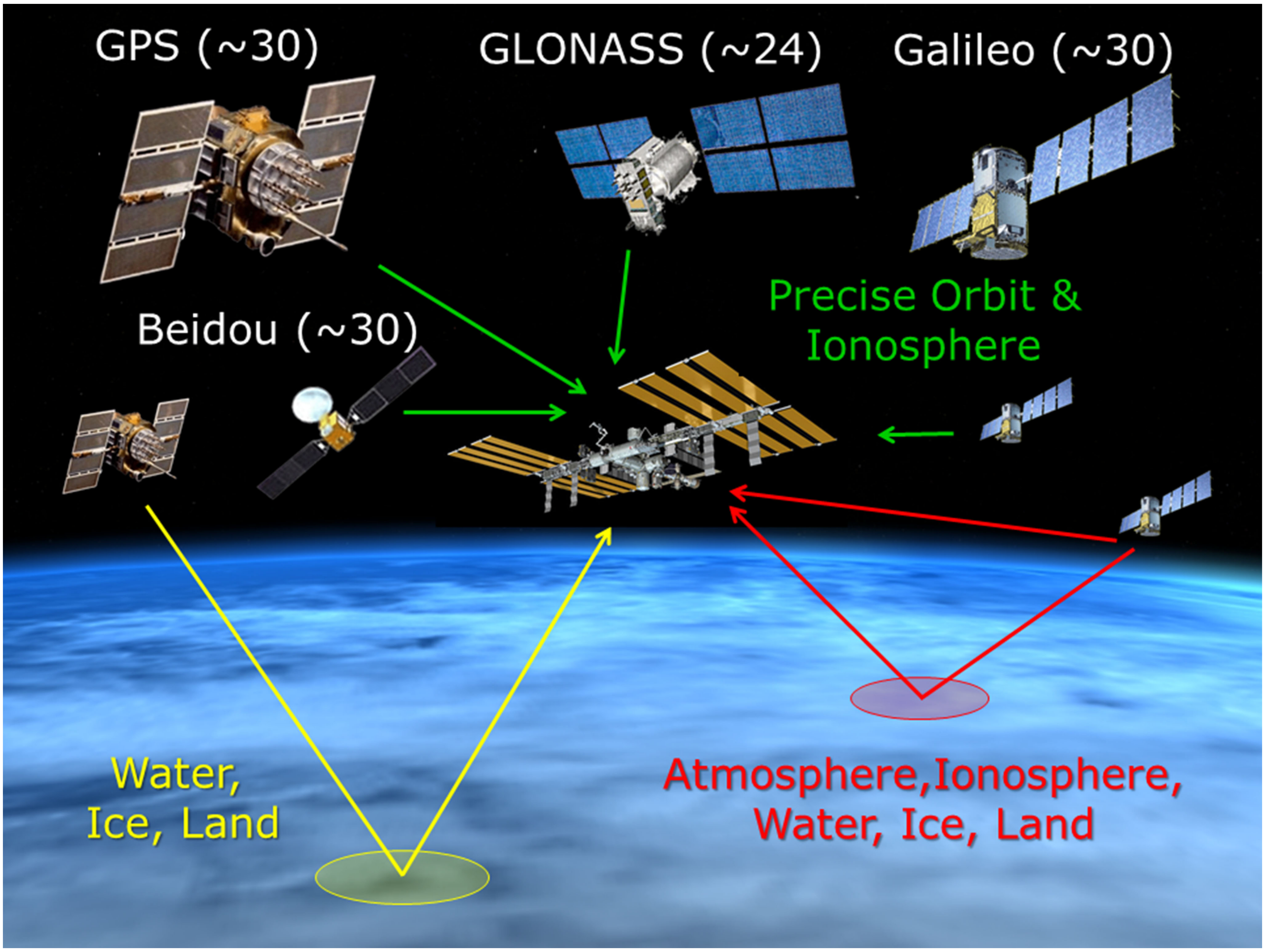

Fig. 1. Schematic overview of the GEROS experiment to be installed aboard the International Space Station. Yellow indicate the reflectometry measurements for water, ice, and land surface monitoring (Field of View 1, see Section III). Red lines indicate coherent reflectometry observations for water, ice, and land surface (Field of View 2) and GNSS Radio Occultation for atmosphere/ionosphere sounding (Field of View 3). The green lines symbolize the GNSS signals, received from above the ISS with the nadir antenna for Precise Orbit Determination (POD) of the GEROS payload and 3-D upside ionosphere monitoring.

(RO) technique and the monitoring of land surface parameters utilizing reflected GNSS signals (see Fig. 1).

Complementing the Earth observations from other current satellite missions, GEROS will especially pioneer the exploitation of GNSS remote sensing signals from the European Galileo system, thereby improving the accuracy as well as the spatiotemporal resolution of the derived geophysical observables compared to GPS only measurements. The additional use of signals from the Russian GLONASS, Chinese BeiDou, and Japanese QZSS navigation satellite systems is also a goal.

GEROS will contribute to the long-term and climate relevant observation of the major components of the Earth system: Oceans/Hydrosphere, Atmosphere/Ionosphere, solid Earth/Landcover, and even Cryosphere/Snow (limited mainly to glacier regions as Himalayas and Andes due to the ISS orbit charcteristics), with innovative and complementary aspects compared to established Earth Observation satellite missions. Therefore, the data from GEROS will allow for climate change-related scientific studies addressing the challenges of ESA's Earth Observation strategy [2], [3].

GEROS will mainly provide mid- and low-latitude observations on submesoscale or longer oceanic variability (see Fig. 2) with focus on coastal regions, surface ocean currents, surface winds, wave heights and the vertical atmospheric temperature, water vapor, and electron density structure for a period of at least two years, preferably longer, depending on the space allocation for the external payloads. The GEROS-RO observations will lead to a better understanding of the climate system, e.g., of ocean barotropic variability, Rossby wave large-scale structures, eddy-current systems, and fronts and coastal upwelling. GEROS hereby takes advantage of the capacious infrastructure aboard the ISS, which is a unique platform for the development of further and advanced GNSS-Reflectometry (GNSS-R) and GNSS-RO techniques, due to minor limitations with respect to, e.g., antenna size or availability of appropriate electric power. Promising applications in that respect are future multismall-satellite constellations for tsunami detection and early warning [4], [5]. Due to the application of these innovative GNSS remote sensing methods GEROS is also supported by the ESA Directorate of Technical and Quality Management (TEC).

GEROS will provide a sensor calibration/validation option for other upcoming satellite missions including, e.g., the European twin platform ocean remote mission Sentinel-3 (with Sentinel-3A launched on February 16, 2016, and Sentinel-3B to

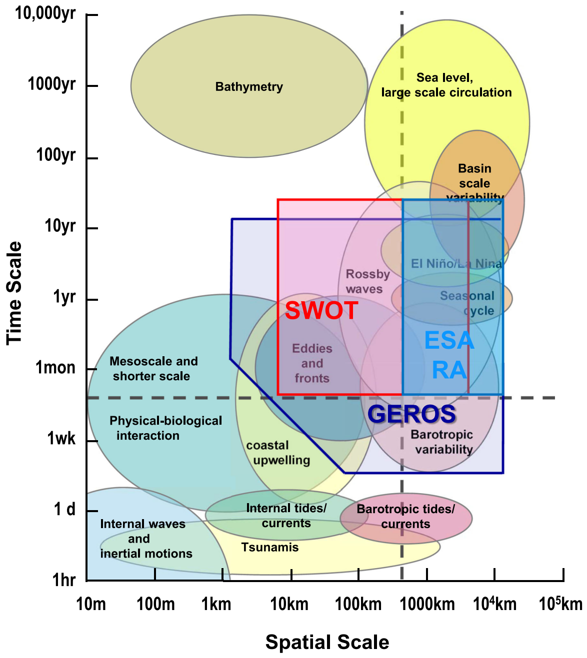

Fig. 2. Oceanic observations carry signals of a wide range of related processes. The observed fingerprints of these processes have temporal time scales from 1 h to thousands of years and spatial scales from ten to tens of thousands of kilometres. The figure illustrates the spatial and temporal scales for these processes and indicates phenomena, which can be investigated with GEROS data complementary to and distinct from, the planned NASA SWOT mission and ESA's and NASA's radar altimetry missions (Redrew and revised from [8]).

be launched in 2017, duration 7–12 years), the U.S./European SWOT (Surface Water Ocean Topography, launch foreseen 2020, with duration three years), and the U.S./Taiwan 12 satellite constellation FORMOSAT-7/Constellation Observing System for Meteorology, Ionosphere and Climate (COSMIC-II) for GNSS-RO (initial launch of six low inclination orbiting satellites planned for 2017, duration at least 5 years). The GNSS remote sensing data from GEROS will also complement the innovative GNSS scatterometry measurements from the U.S. mission CYGNSS (CYclone Global Navigation Satellite System), which was selected by NASA's Earth System Science Pathfinder program and is currently foreseen for launch in late 2016. CYGNSS (eight small satellites, [6]) will study the relationship between ocean surface properties, moist atmospheric thermodynamics, radiation and convective dynamics for the investigation of tropical cyclones. [7]

After introducing the mission (see Section II), we briefly review the technical concept (see Section III). In Section IV, we present the structure and initial results of the GEROS-SIM (GEROS-SIMULATOR), developed by an international science team in cooperation with ESA. To complete the paper we present selected scientific results of the ongoing GEROS preparation phase (Section V), followed by a summary and outlook (Section VI).

II. GEROS MISSION

A. *Mission Goals*

The primary mission objectives of GEROS are [9] the following:

1) To measure and map altimetric sea surface height (SSH) of the ocean using reflected GNSS signals to allow methodology demonstration, establishment of error budget and resolutions and comparison/synergy with results of satellite-based nadir-pointing altimeters. This includes precise orbit determination (POD) of the GEROS payload.
2) To retrieve scalar ocean surface mean square slope (MSS), which is related to sea roughness, wind speed and direction, with a GNSS spaceborne receiver to allow methodology testing, establishment of error budget and resolutions. In addition, two-dimensional MSS (directional MSS, related to wind direction) would be desirable.

Hereby GEROS will be the first GNSS-R mission with the capability for mesocale ocean altimetry, which was also the main idea behind the original mission proposal [1]. The capability to sample oceanic mesoscale eddies is a driver of any new altimetric mission. As derived from these observations, the ocean circulation monitoring and its forthcomming improvements shall rely on the mapping of the complex structures of the surface velocities (∼10–100 km or longer) in less than few days in the open ocean and in the coastal regions. Therefore, we believe that the need to widen the coverage in terms of spatial and temporal scales—as compared to the Sentinel-3 (ESA) and the planned SWOT (CNES/NASA) missions—is to be tackled by other missions. One of the objectives of GNSS-R global observations is to quantitatively contribute to fill-in the 100 km "altimetry temporal gap" by combining conventional altimeter data with GNSS-R measurements much denser in time. It has been shown that these additional observations are appropriate to address the mesoscale sampling capability, although the measurement performances are not comparable with the state-of-the-art in altimetry. In particular, the GNSS-R added-value is based on its resolving capability, i.e., the ability to resolve the signal regionally or globally by tracking the mesoscale ocean features. It can nicely complement the ability to observe submesoscale structures, that should be properly addressed by the future high-resolution altimetric missions using Doppler or wide-swath measurements.

Secondary mission objectives, which increase the scientific value of the GEROS data, but are not driving the instrument developments, include

1) to further explore the potential of GNSS-RO data (vertical profiles of atmospheric bending angle, refractivity, temperature, pressure, humidity, and electron density), particularly in the Tropics, to detect changes in atmospheric temperature and climate relevant parameters (e.g., tropopause height) and to provide additional information for the analysis of the reflectometry data from GEROS and
2) to assess the potential of GNSS scatterometry for land applications and in particular to develop data products such as soil moisture, vegetation biomass, and mid-latitudes snow/ice properties to better understand anthropogenic climate change.

B. *Mission Status*

GEROS was selected in result of a complex review process, initiated by ESA. The review results and decision on further activities were officially announced in the end of 2012. An interdisciplinary and international Science Advisory Group (SAG) of acknowledged experts in oceanography, geodesy, atmosphere, and GNSS science started to work in June 2013 on details of the preparation of the GEROS mission. This SAG consists of key members of the proposing GEROS team and additional experts, nominated by ESA. It cooperates closely with the ESA GEROS team. The first important task of the SAG and ESA, the definition of the initial version of the GEROS Mission Requirements Document, was finished in mid-November 2013 [9]. The first baseline of System Requirements [10] was given in December 2013. The GEROS-SAG is closely linked to other GNSS-R-related missions, e.g., CYGNSS (planned launch late 2016, [6]), TechDemoSat-1 (TDS-1, launched July 8, 2014, [11]), 3Cat-2 (launched August 15, 2016, [12]) and the E-GEM project (European GNSS-R Environmental Monitoring, 2014–2017, [13]). Two external experts from U.S. support the work of the GEROS-SAG and directly contributing NASA's and international scientific interest in GEROS.

Two competitive industrial Phase A studies were started in November 2014 for the GEROS mission implementation and finished in April 2016. These studies were led by Airbus Defense and Space (ADS, Madrid, Spain) and Thales Alenia Space (Rome, Italy).

In parallel the scientific study GARCA (GNSS-R Assessment of Requirements and Consolidation of Retrieval Algorithms), which is also funded by ESA [14], was also started in November 2014 and finished in October 2016. GARCA is performed by 17 scientists, GNSS-R experts and oceanographers, from 7 institutions in 6 European countries (France, Germany, Norway, Portugal, Spain, U.K.). The team is supported by the work of 12 external experts from Denmark, Germany, Italy, Sweden, Switzerland, and U.S. The main goal of GARCA is to support the assessment and consolidation of scientific requirements and the consolidation of retrieval algorithms for a spaceborne GNSS-R experiment, focusing on the GEROS concept and its primary and secondary data products (SSH and ocean surface roughness). The main GARCA work is the development of an end-to-end simulator for the GEROS measurements (GEROS-SIM), and the evaluation of the expected geophysical data products. Additional work packages are included, aimed to assess the oceanographic significance of the expected GEROS measurements by means of Observing-System Simulation Experiments (OSSE). The external scientific experts support the GARCA project and are involved in the work to test the developments and also to initiate the sustainable formation of an interdisciplinary GEROS user community. The scientific results of GARCA were published by the international project team in six technical notes ([15]–[20]). These documents describe in detail the GEROS-SIM and its test and performance.

ESA initiated two flight campaigns in the Baltic Sea not far from the Finish coast line at Helsinki in May 2015 as a proof-of-concept for the altimetric GNSS-R approach foreseen for GEROS. Results from these campaigns are introduced in Section V-A.

The finalization of the industrial Phase A studies in March 2016 and the GARCA study in October 2016 will end with the decision from ESA on the continuation of GEROS in Phase B. As defined in the ISS Strategic Plan, GEROS deployment is foreseen between September 2019 and March 2020 in case of successful preparative studies and provision of appropriate funding. The launch is planned from the Kennedy Space Center (KSC) with a Dragon C3-1 launcher from Space-X and will be followed by a short commissioning phase period. A minimum lifetime of one year is expected, an extension is targeted up to 5 years. Selected mission parameters are summarized in Table I.

TABLE I
GEROS: SELECTED MISSION SPECIFICATION PARAMETERS AS OF SEPTEMBER 2016

Orbit altitude:	375–435 km
Inclination:	51.6°
Orbit period:	∼92 min
Planned Launcher:	Dragon C3-1 Space-X
Planned Launch site:	Kennedy Space Center
Planned Launch year:	2020
Planned Mission duration:	Min. 1 year with possible extension up to 5 years
Payload mounting at ISS:	Columbus external payload facility (box $117 \times 86 \times 155$ cm^3), upper balcony
Operation:	power ≤ 500 W, downlink ≤ 1 Mbps

III. TECHNICAL CONCEPT

This section presents the results of one of the industrial Phase A studies as an example of the technical solution found for the GEROS mission which satisfies the mission requirements set by the scientists [9].

A. *Operational Concept*

GEROS will be integrated onto the Columbus External Payload Adapter (CEPA), in turn attached to the Active Flight Releasable Attached Mechanism of the Space-X Dragon's unpressurized trunk. At KSC, the trunk will be assembled to the Dragon's capsule and launched into space by a Falcon 9 booster. During the transit flight to the ISS the GEROS payload will be exposed to the space environment. Dragon will approach the ISS to be captured by the Space Station Remote Manipulator System for docking. The Special Purpose Dexterous Manipulator will grab and remove GEROS out of Dragon's trunk, to move it to the Starboard Overhead, X-direction location (EPF-SOX) of the Columbus External Payload Facility (CEPF). Installed at this position, the GEROS payload will perform its nominal operation. At the end of the mission, the reverse sequence will be followed to embark GEROS back into the trunk of another Dragon vehicle for a destructive reentry. During operation, the Columbus module will provide power to GEROS, and through the multipurpose computer and communications system, a data link for telemetry, tracking and command and scientific data transfer to and from ground. One of the ISS User Support and Operation center will be used as interface node to the Science Support Center (SSC), in charge of the payload command, operations and data processing (at both Levels 1 and 2). The GEROS payload is expected to run on weekly plans prepared in advance at the SSC and then uploaded. The European Space Astronomy Center has been proposed as SSC for this center will host an archive of Galileo science exploitation data.

B. *GEROS Payload*

The key GEROS payload is a beamforming antenna (GAB, GEROS Antenna Beamformer), which has 4π steradian field of view (FoV) capability to receive GNSS signals arriving from any direction. The half space is however masked by the structure of the Columbus module so that only starboard azimuth angles

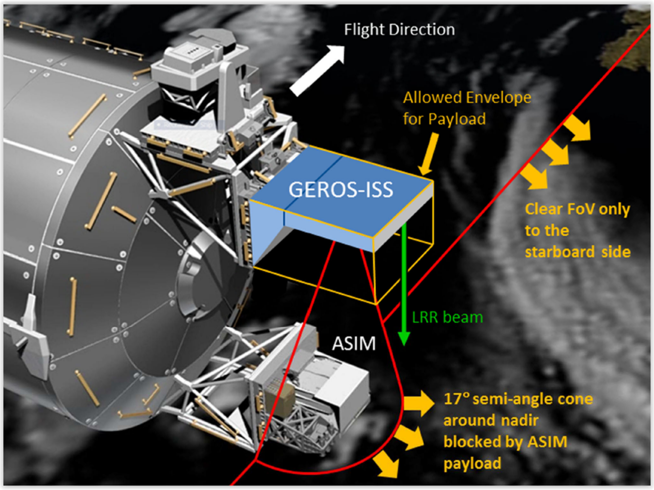

Fig. 3. GEROS deployment at the upper Columbus External Payload Facility "upper balcony" of the ISS Columbus module with limited field of view (credits ESA).

between 0° (velocity) and 180° (anti-velocity) are really accessible. In elevation, the nadir angle ranges from 0° (nadir) to 90° (antenna horizon) but the FoV is blocked for values below 17° byAtmosphere-Space Interactions Monitor, the payload in the CEPF location just below GEROS (see Fig. 3).

Ignoring other less important blockages like those produced by the main truss and the rotating solar wings, Fig. 4 depicts the resulting FoV accessible to the GAB. Three distinct parts are distinguished within the GEROS FoV involving near nadir reflections (FoV-1) for altimetry and scatterometry, grazing reflections for altimetry (FoV-2), and RO (FoV-3) for atmosphere/ionosphere sounding. FoV-1 comprises nadir angles from 17° till 41°, corresponding to direct signals with zenithal angles between 20° and 50°. The FoV-2 nadir angle range is between 54° and 69°, corresponding to direct signals between a zenith angle of 68° and a nadir of 80°—GNSS satellites at the antenna horizon generate specular point at a nadir angle of 65°. Finally, the FoV-3 comprises the first 250 km of the atmosphere spanned by nadir angles between 69° (Earth surface) and 77° .

The right panel of Fig. 4 shows the antenna directivity, averaged over azimuth, at frequency bands F1 (1547.1–1594.5 MHz, with center frequency at 1,570.8 MHz, solid line) and F5 (1157.4–1221.3 MHz, with center frequency at 1189.3 MHz, dashed line) as a function of zenithal and nadir angles. The antenna directivity at zenith (and nadir) is 24.5 dB at F1 and 22.5 dB at F5, rolling down some 3–4 dB at the edge of FoV-1. The directivity within the FoV-2 varies from 3 to 19 dB depending mainly on the location of the specular point. The directivity in FoV-3 is between 14 (toward the troposphere) and 10 dB (top of the atmosphere).

The visibility analysis performed (see Section IV-A) concluded that the optimum number of antenna beams for the GEROS payload was 4 because this is the amount of near nadir, grazing, and RO events, altogether, that will happen simultaneously most of the time, when considering a realistic set of GNSS satellites expected to be in orbit in the 2020–2024 time frame. The way the four beams are arranged in frequency and polarization for the various applications is shown in Fig. 5. The GEROS payload can track, in parallel, three direct signals in right-handed circular polarization (RHCP) and the corresponding three near nadir reflected signals in both RHCP and left-handed circular polarization (LHCP), at F1. The same capability is available at F5 but only in LHCP polarization for the near nadir reflected signals. An additional fourth dual-frequency beam set can be used to observe either a fourth near nadir reflection, a grazing reflection, or a RO event. The GEROS payload provides yet an additional configuration for precipitation observations in which the fourth dual-frequency beam set is used to receive an occultation in both polarizations.

When the fourth dual-frequency beam set is used for grazing altimetry, the beam configuration depends on whether the corresponding direct signal is received from the zenithal or the nadir space. In either case, it is the RHCP polarization at frequency band F5 which is processed. Grazing altimetry is performed in GEROS by implementing the master–slave technique in [21] but taking the direct signal as the master signal.

The bandwidth of the GEROS payload is of 47 MHz at F1, and 64 MHz at F5. The two reception bands F1 and F5 are placed to maximize the number of GNSS signals which can be observed. As shown in Fig. 6, GEROS can perform GNSS-R and RO with a wide variety of signals from different GNSS systems, including GPS, Galileo, GLONASS, BeiDou, QZSS, and their augmentation systems MSAS, WAAS, EGNOS, and IRNSS.

The main Level 1 output of the GEROS payload is provided at 1 s output rate and is depicted in Fig. 7. For three of the beam sets, it consists of three delay Doppler maps (DDM) with a particular sampling of the 1500 m, 8 KHz delay-Doppler domain and polarization combination. Each of the solid lines in Fig. 7 represents a 400 delay lag waveform at a specific Doppler obtained at a high delay resolution of 3.75 m. The dashed lines correspond to 133 delay lag waveforms with a lower delay resolution of 11.25 m. There is a maximum of nine Doppler lines in each DDM, whose location is programmable. The specular point is nominally located at delay lag 600 m. The three DDMs are provided both in power, after an internal incoherent accumulation has taken place, and in complex form, obtained by only coherent integration. These three DDMs constitute the observables to perform near nadir altimetry and scatterometry.

The Level 1 data produced from the fourth beam set depends on the application. When used for near nadir altimetry and scatterometry the output data are the one just described. When used for one of the special applications, the output data rate for this specific beam set is increased to 20 Hz, and consists of two 11.25 m resolution 900-m long delay waveforms (80 delay lags), at F1 and F5, with a polarization combination according to the observation: RHCP × RHCP for grazing altimetry and RO, and RHCP × LHCP for precipitation. These waveforms are provided only in complex form.

The GEROS payload is shown in Fig. 8. Its overall dimensions are 1.55 m × 1.17 m × 0.86 m. Its most prominent feature is the antenna (green array in Fig. 8), a double-face GAB, with 30 elements on each side (zenith and nadir). An additional element, right at the center position in the zenith array, is used only for POD. Similarly, a laser retro-reflector is placed at the central nadir position for POD verification (see the grey element in Fig. 8). In between the two faces of the antenna are the calibration and low noise amplifier units. These units

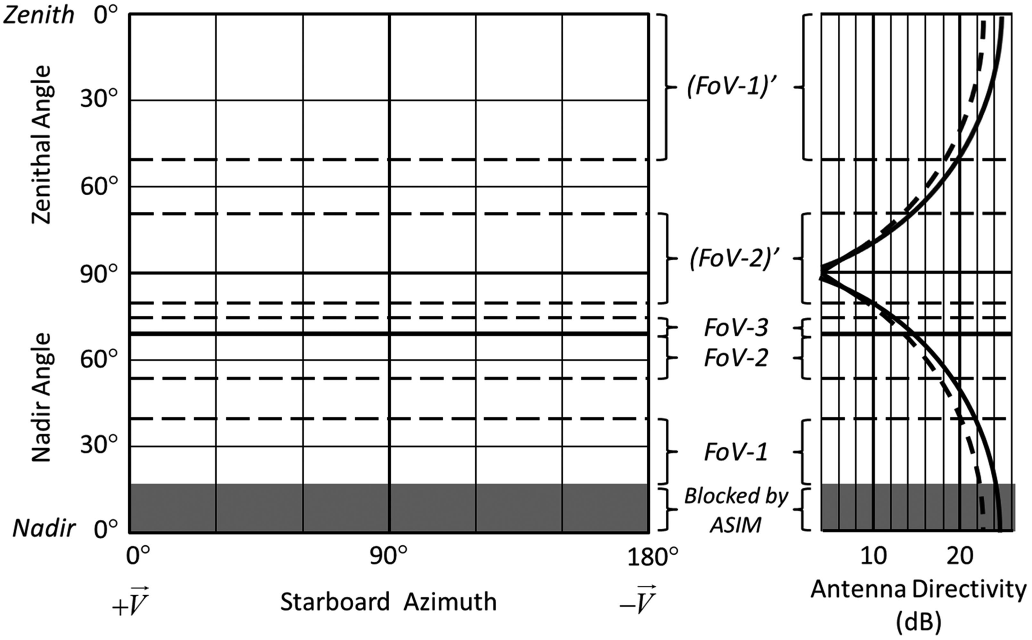

Fig. 4. The left panel shows the Field of View (FoV) of the GEROS payload: FoV-1 corresponds to near nadir reflections; FoV-2 to grazing reflections; FoV-3 to radio occultation; the primed FoV-1 and FoV-2 correspond to the respective direct signals. The right panel presents the antenna directivity at frequency bands F1 (1,570.8 MHz, solid line) and F5 (1,189.3 MHz, dashed line) as a function of the zenith and nadir angles (antenna directivity is relatively constant for all azimuth angles).

perform the critical functionality of routing both the direct and reflected signals through the same receiving chain, referred to as the swapping technique. This way the GEROS payload is self-calibrated in delay and amplitude (except for the antenna patterns).

The GAB signals are routed into six identical beamformers (see orange boxes below the antenna in Fig. 8): three beamformers at F1 for the direct RHCP signals, and the reflected signals at RHCP and LHCP polarizations, and a similar set at F5. The output from these beamformers consists of the 21 beams depicted in the left upper panel of Fig. 5, which are routed to 2 identical signal processing units (SPU).

The two SPU are sitting in the two inner corners of the payload (see blue boxes below the beamformer units in Fig. 8). They are in charge of the analog to digital conversion and signal correlation. With the help of modeled delays, the SPU can delay direct signals to match the reflected ones to perform interferometric GNSS-R, useful for near nadir and grazing altimetry as well as scatterometry. Clean replicas are generated on board for RO, which can also be performed with the interferometric approach. The implementation of the SPU is based on a specifically designed PARIS Correlator (PACO) digital circuit. Another important function of the SPU is to blank the input signal when there is interference, a likely situation in F5 due to the distant measurement equipment used by civil aviation radars. The output of the SPU are the set of DDM described earlier.

Other additional units of the GEROS payload shown in Fig. 8 are the instrument control unit (ICU, in light green), the power supply unit (PSU, in red) and the POD GNSS receiver (POD, in yellow). The GEROS payload is mounted on the CEPA tray, which provides all necessary interfaces to the Columbus module. The GEROS payload has a total mass of 376 kg (with 20% margin), 395 W (with 20% margin), a 2 GB mass memory (80% storage capacity) and a 1.2 Mbps output data rate.

C. Instrument Error Budget

The GEROS payload is very similar to the PARIS IoD one [22]. During the PARIS IoD Phase A activities, a detailed instrument optimization and error budget was performed [23]. It included for each band, the effect of thermal and speckle noises, coherent and incoherent averaging, and the signal-to-noise ratio (SNR) degradation due to antenna losses, amplitude and phase errors in the beamformer, antenna phase center error, receivers noise figure, frequency response mismatch (bandwidth and group delay), quantization efficiency, and the delay and Doppler refresh rate retracking updates, with the help of an ad hoc end-to-end simulator that evolved from the passive advanced unit (PAU) end-to-end simulator [24]. The error budget was later improved by computing the Cramer–Rao bound (CRB, [25]). Fig. 9 shows the computed performance for the Galileo signals. The altimetric error increases with wind speed and the cross-track distance from the nadir. It shows the advantage of the interferometric GNSS-R (iGNSS-R) in terms of the altimetric performance, as comparing the lines of σ_{iF} with those of σ_{cF} in Fig. 9.

IV. GEROS-SIMULATOR

One of the key parts of the GARCA study is to implement an end-to-end simulator covering from detailed instrumental aspects to higher level data products useful to assess GEROS oceanographic impact in the current or near-future Earth Observation System. It includes the simulation of GNSS-R observables (Product Level 1, L1), a large suite of extraction

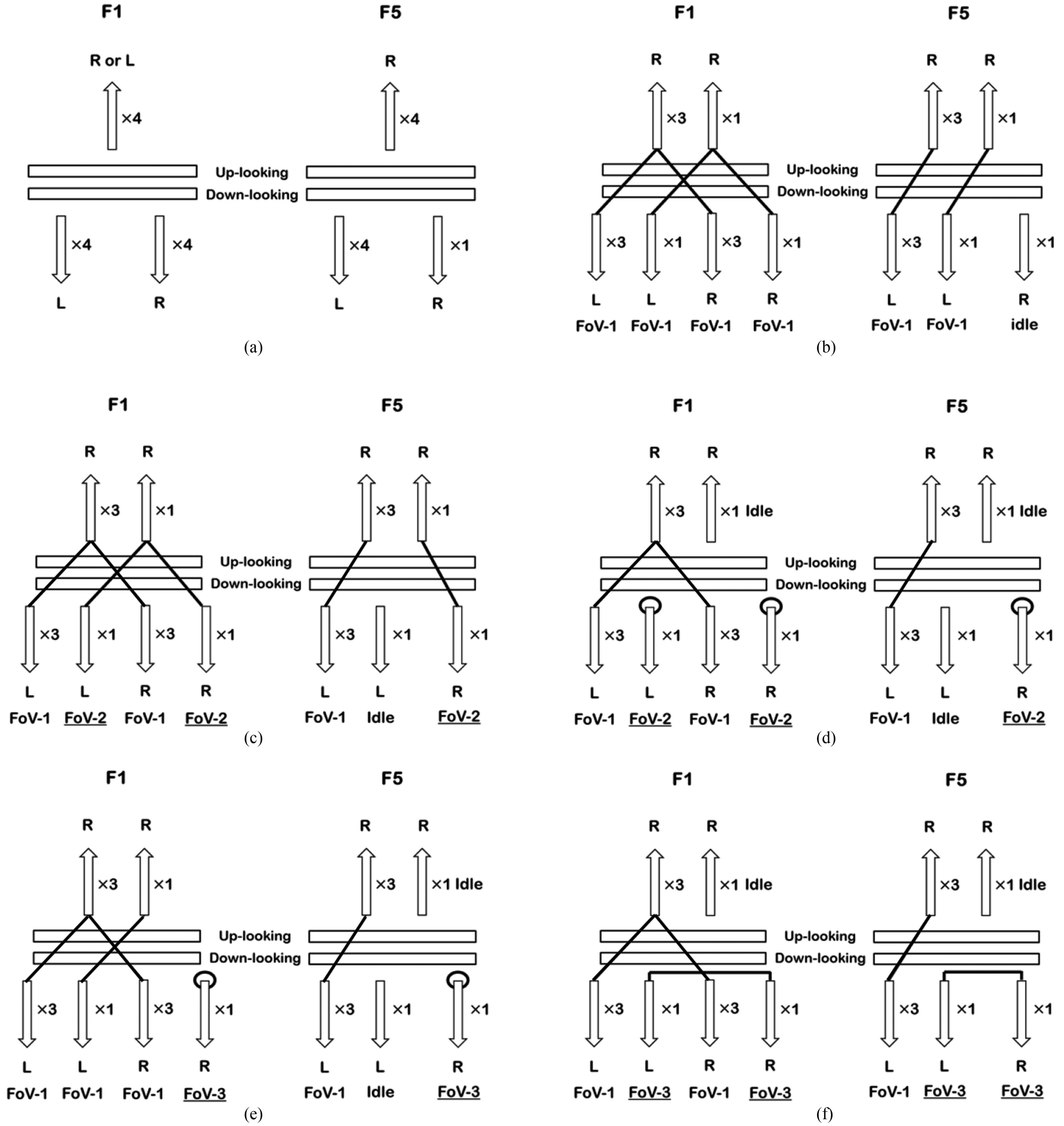

Fig. 5. Schematics of the GEROS payload beam configuration. Thick lines indicate cross-correlation pairs or autocorrelation. The left column presents (top to bottom) (a) beams, frequencies, and polarizations (R = RHCP, L = LHCP), (b) near nadir altimetry and scatterometry, and (c) same as (b) but with one beam used for grazing altimetry with the direct signal in zenith. The right column presents (top to bottom) (d) same as (c) but the direct signal in nadir, (e) the same as (d) but using one beam for radio occultation instead of grazing altimetry, and (f) same as (e) but using one beam for precipitation observations.

algorithms to generate geophysical products (Product Level 2, L2), their time- and geo-location, and noise and systematic effects. The GEROS-SIM consists of a core of modules which produce the GNSS-R observables from detailed geometric and instrumental parameters, plus a series of other modules with well-established input/output interfaces to generate all the other steps. Each of the modules runs independently of the others if the right input data format is provided. The advantage of this approach is that the different L1-to-L2 modules can be used as retrieval algorithms also for real experimental data, if these are provided in the right format. Consequently, the modules, developed within the GARCA project, provide already the initial version of the potential GEROS processor for the generation of the geophysical Level 1 and 2 data products (see Section IV-F) to serve the primary mission objectives (see Section II-A) altimetry (code and phase) and scatterometry. Fig. 10 provides a schematic view of this processor. In this section, each simulator module is briefly explained with some

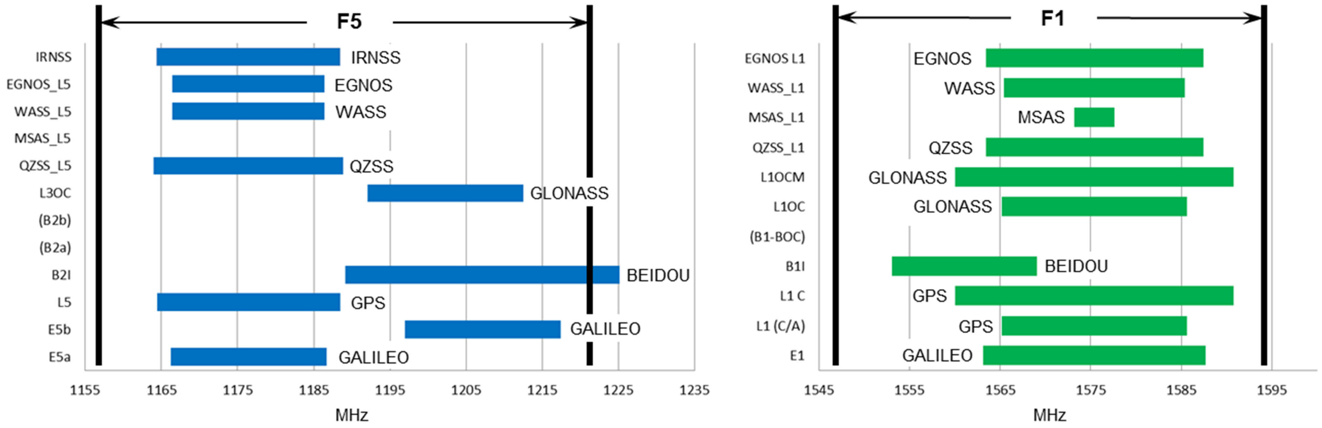

Fig. 6. GNSS signals which can be processed by the GEROS payload for GNSS Reflectometry and radio occultation within its two frequency channels, F1 and F5 (Courtesy: ADS-CASA).

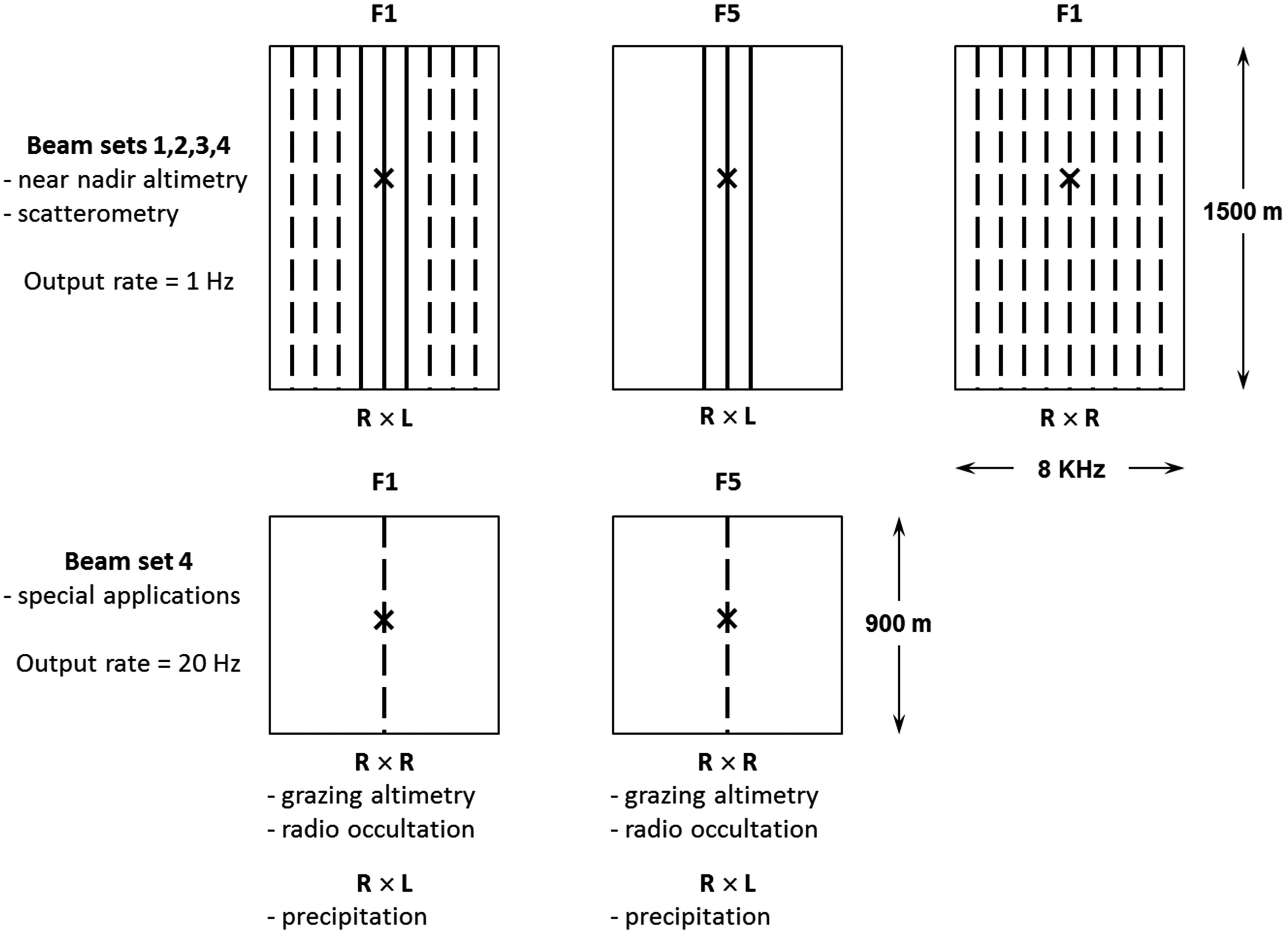

Fig. 7. Delay Doppler maps (DDM) are provided by GEROS-ISS every 1 s. The output from beam 4 depends on the application it is being used for. The DDM domain is limited within 1500 m, 8 KHz or 900 m, 8 KHz depending on application. The cross indicates the nominal position of the specular point. Each line represents a waveform along delay for a specific Doppler frequency. The delay resolution is 3.75 (solid lines) and 11.25 m (dashed lines). The position of all Doppler lines can be programmed. The set of all DDMs is given in power (except for special applications) and in complex form in parallel.

examples of simulation results, which are described in detail in [18].

A. Simulation of GEROS Observation Coverage

The GEROS-ISS observation modes are defined according to the GEROS mission objectives (see Section II-A for three different FoVs; see Figs. 3 and 4 and Section III-B). As a requirement, the payload should be able to track beams with incidence angles up to 80°, for both up- and down-looking antenna arrays. The GEROS simulator performs the geolocation of the specular points. It includes the ESA Earth Observation Customer Furnished Items (CFI) software [26] for accurate timing, coordinate conversions, antenna pointing, and reflections

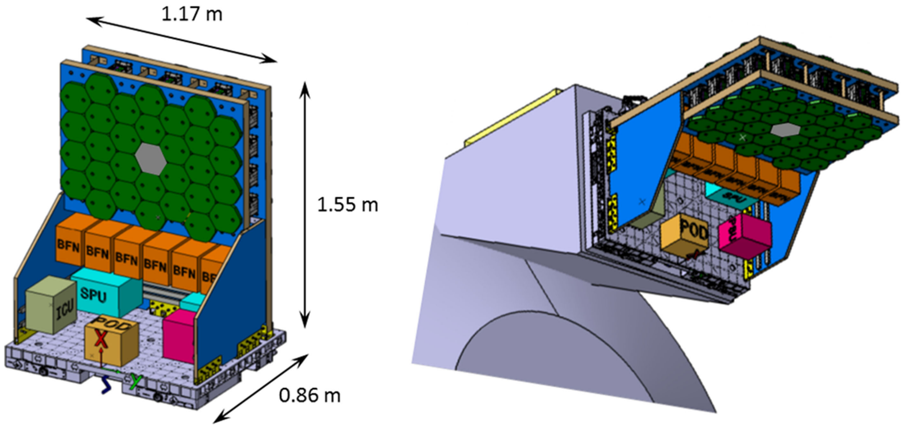

Fig. 8. GEROS-ISS payload (left) accommodated on the upper CEPF of the Columbus module (right). (Courtesy: ADS-CASA)

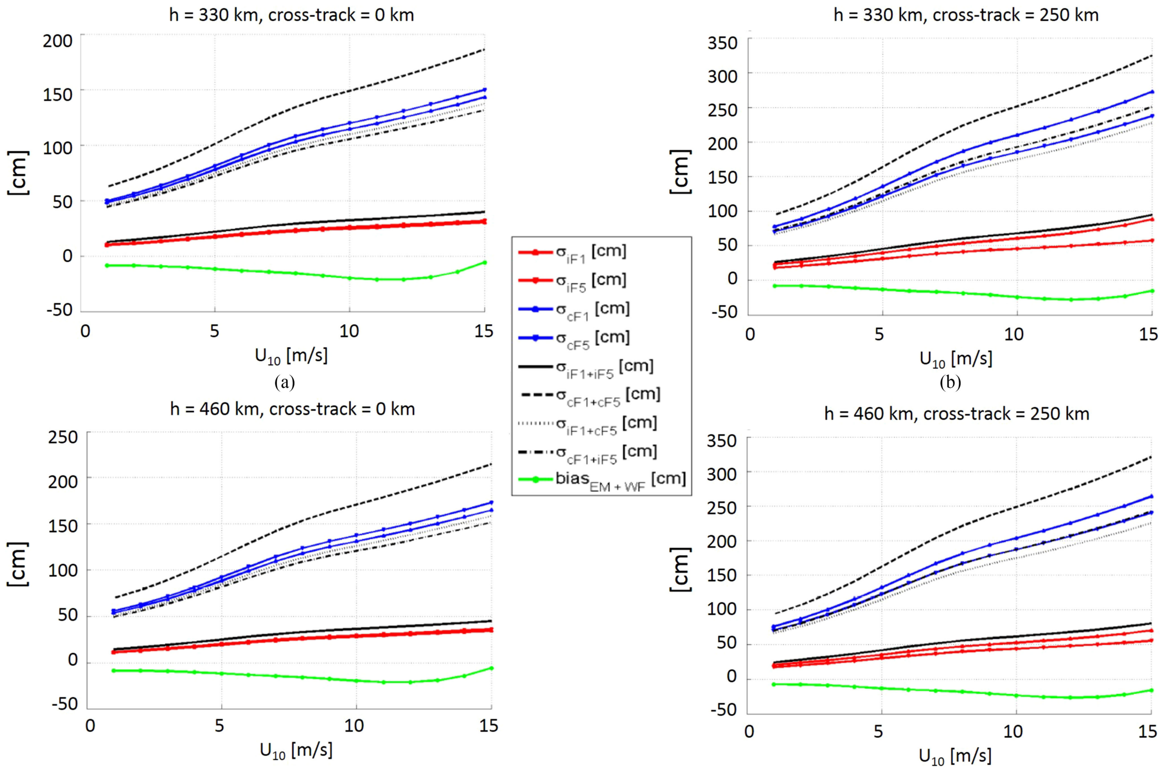

(a) (b) (c) (d)

Fig. 9. GEROS instrument 1-s integrated rms errors (σ) as predicted by theoretical CRB techniques using Galileo signals for the cases of ISS height 330 km (a, b) and 450 km (c, d). The figures in left column (a, c) show the result for cross-track distance 0 km, and ones in the right column (b, d) are for 250 km cross-track distance. The legends denote iF1 (E1 interferometric), iF5 (E5 interferometric), cF1 (E1 conventional), cF5 (E5 conventional). The bias denotes total bias (electromagnetic and waveform bias).

calculations. The simulations for this study used a 30 days period with 10 s sampling.

The GNSS systems, predefined for the calculations in GEROS-SIM are the following:

1) BeiDou including 35 satellites (5 in GEostationary Orbit, GEO; 3 in Inclined GeoSynchronous Orbit (IGSO); and 27 in Medium Earth Orbit (MEO)),
2) Galileo including 30 MEO satellites (24 operational + 6 spares),
3) GLONASS including 24 operational MEO satellites,
4) GPS with 31 MEO satellites (24 core + 7 extra), and
5) QZSS with 3 satellites (1 in IGSO; and 2 in GEO).

The ISS orbit is set with an orbit altitude of 400 km and a revolution of 90 min. The figure below (see Fig. 11) shows the resulting distribution of the GEROS measurements and the average revisit time for FoV-1 [27].

Due to technical limitation of the payload, the observations are limited by the number of beams, which can be tracked by the GAB (see Section IV-B). For near nadir FoV-1, four beams are in view more than 80% of the time, with 50% of the measurements lower than 33° incidence (see Fig. 12).

For FoV-2 (grazing angle), an update in the system requirements during the GARCA scientific assessment, allowing the use of the up-looking antenna, made a great improvement in

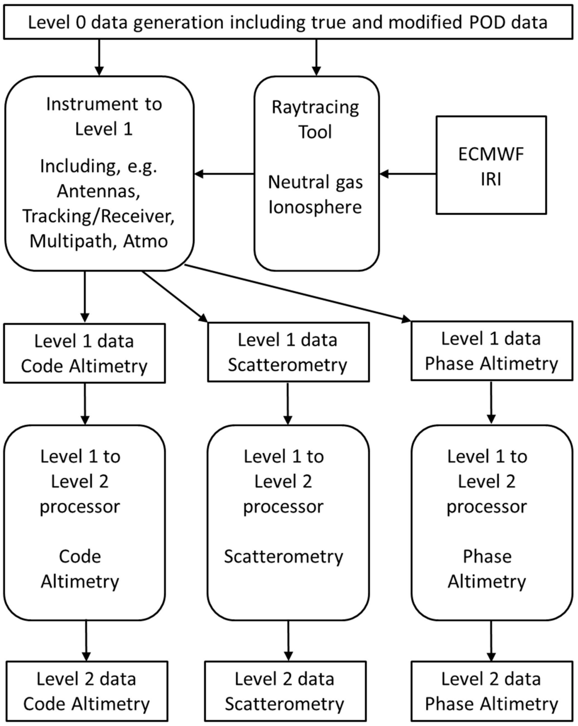

Fig. 10. Schematic overview of the GEROS-SIM. The developed module "Instrument to Level 1" and the three modules "Level 1 to Level 2 processor" provide already the core of the potential GEROS processor for the primary mission data products (see Section IV-F).

the number of beams that can be simultaneously observed, where now 4 beams are in view more than 97.7% of the time (see Fig. 13). About 24% of the beams pairs coming from the down-looking antenna only, while 76% use the up-looking antenna to track the direct signal and the down-looking tracks the reflected one. The plateau in the cumulative incidence angle distribution, observed in Fig. 13 (right), shows this up–down transition in the direct signal tracking, limited in the limb direction by the antenna beamformer maximum incidence angle of 80° (see Fig. 4).

B. *Instrument to Level 1 Processing*

This module includes algorithms to generate GEROS-SIM instrument measurements (L0) and corresponding L1 data. Using the inputs of observation geometry, sea surface state, and instrument hardware specification, it computes the observable DDM/Waveforms [28]. For efficient implementation, an established GNSS-R simulator, PAU/PARIS E2E Simulator (P2EPS) [24], [29] has been largely reused by adapting to the particular GEROS specifications, which are antenna array beamforming, receiver effect, tracking, and noise characteristics, etc.

One particular difference of GEROS from other spaceborne GNSS-R instruments (e.g., TDS-1 and CYGNSS) is the antenna array beamforming capability. To increase the SNR, GEROS is capable of pointing the antenna beam to the specular reflection point. GEROS-SIM also provides this function for analyzing the impact of pointing error. Fig. 14 shows a simple demonstration of the pointing error. The error of 10° in Fig. 14(c) causes a serious degradation of DDM shape as shown in Fig. 14(d). We note, that the ISS attitude can vary up to $\pm 15^\circ$ per axis. However, variations are typically around 1° per axis per orbit (maximum 3.5° per orbit). The typical attitude variations are much smaller that the antenna beamwidth (of about 11° or wider) and hence do not prevent pointing the antenna beams toward the GNSS satellites or the specular points.

The GEROS-SIM algorithm of DDM generation is based on the efficient DDM computation method [30]. This method is known as a fast and efficient computation version of the Zavorotny–Voronovich model [28]. This baseline algorithm was used for P2EPS, and was validated as comparison to spaceborne (UK-DMC) and airborne measurements (PIT-POC) [31] the latter including the interferometric GNSS-R approach. Additionally, the GEROS-SIM has been validated using the 57 samples of TDS-1 data. Examples for these comparison between TDS-1 and GEROS-SIM DDMs are shown inFig. 15. More detailed results of validation test are reported in [18].

C. *Level 1 to Level 2 Processing*

In this section, we describe the three processing modules and test results for the generation of the primary GEROS geophysical data products. SSHs are derived using the code and phase altimetry approach, which are treated separately and were developed by IEEC and GFZ, respectively. Surface roughness and wind observations are generated with the scatterometry processing module, developed by NOC.

1) Code Altimetry: The interferometric GNSS-R technique provides the cross-correlation between the signal received through the zenith-looking antenna system and the nadir-looking one. The zenith-looking antenna collects the signals directly propagated from the transmitter to the receiver, while the nadir-looking system acquires the signals reflected off the Earth surface. If the reflection were generated by a smooth mirror-like surface, the cross-correlation of both branches of the signal would result in the autocorrelation function of the transmitted signals, with its peak delayed as $\Delta\rho = \rho_R - \rho_D$, where ρ accounts for the propagation time between signal transmission and signal reception, whereas subindexes $_R$ and $_D$ state for specular reflection radio-link and direct radio-link, respectively. As explained in Section IV-B, the roughness of the surface is an input parameter of the simulator, as it distorts the shape of the cross-correlation function, also called waveform. Unlike reflections off smooth surfaces, the delay of the peak of the distorted waveform does not correspond to the delay of the ray-path reflected at the specular point, as diffuse scattering around the specular point tend to add further delayed contributions to the received signal. How is it then possible to estimate the delay of the specular point? Which point along the waveform must be used as reference for the specular point reflected signal? Different possibilities have been suggested in the literature, such as fitting a model of the waveform so the information about the specular point delay is embedded in the fit (e.g., [32]), using the peak of the first derivative of the leading edge as delay of the signal reflected at the specular point (e.g., [33]–[35]), or the delay of an intermediate power-value [35], [36]. The code delay algorithm implemented in the GEROS-SIM identifies the peak of the leading edge derivative (LED) as the specular delay. The LED is computed on the central Doppler slice of the DDM,

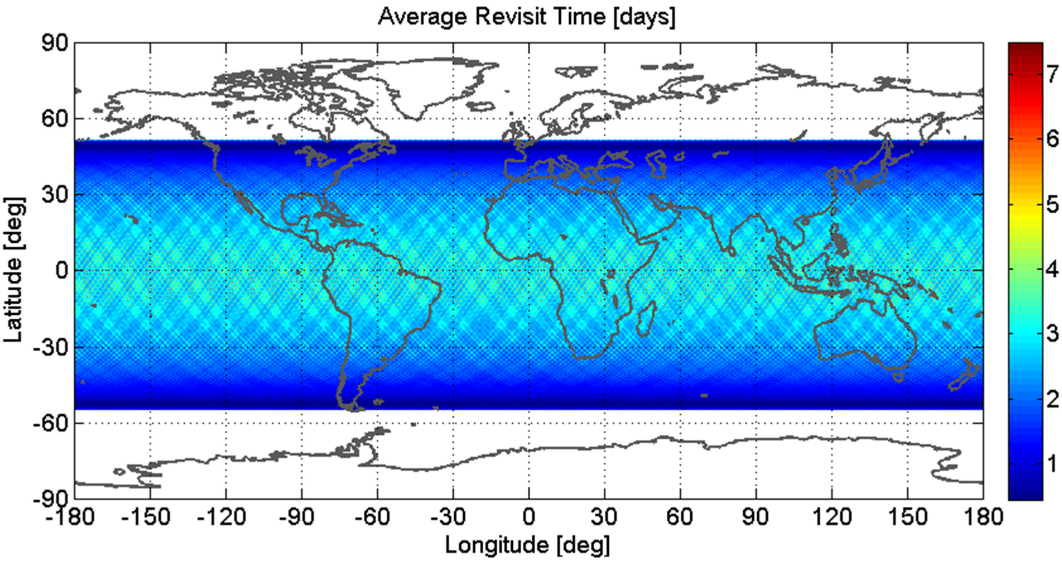

Fig. 11. ISS observation coverage and average revisit time for near nadir observations, FoV-1 [27].

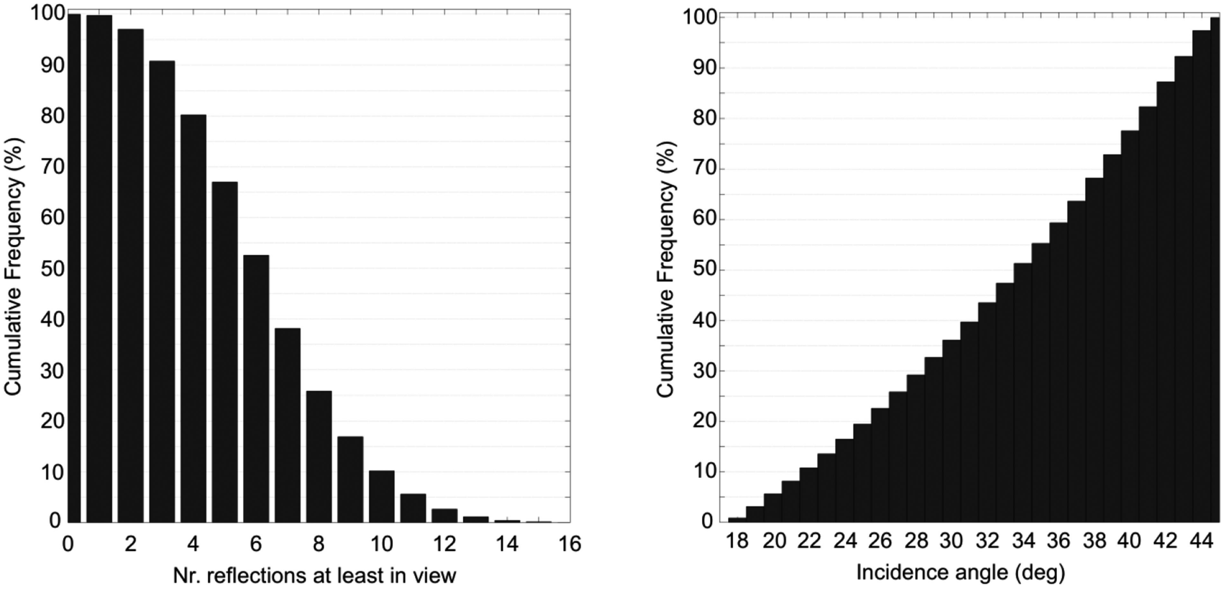

Fig. 12. GEROS FoV-1 cumulative distribution of the number of beams (left) and incidence angles (right).

that is, the slice that corresponds to the Doppler frequency of the specular point. Then, the measured delay, $\Delta\rho_{\text{LED}}$, has the following terms:

$$\begin{aligned}
\Delta\rho_{\text{LED}} &= \rho_R - \rho_D \\
&= (\rho_R^{\text{geo}} + \rho_R^{\text{tropo}} + \rho_R^{\text{iono}} + \rho_R^{T-\text{clk}} + \rho_R^{R-\text{clk}} + \rho_R^{\text{instr}} \\
&\quad + \rho_R^{\text{shape}} + \epsilon_R) \\
&\quad - (\rho_D^{\text{geo}} + \rho_D^{\text{tropo}} + \rho_D^{\text{iono}} + \rho_D^{T-\text{clk}} + \rho_D^{R-\text{clk}} + \rho_D^{\text{instr}} \\
&\quad + \rho_D^{\text{shape}} + \epsilon_D) \\
&= \Delta\rho_{\text{geo}} + \Delta\rho_{\text{tropo}} + \Delta\rho_{\text{iono}} + \Delta\rho_{T-\text{clk}} + \Delta\rho_{\text{instr}} \\
&\quad + \Delta\rho_{\text{shape}} + \epsilon \qquad (1)
\end{aligned}$$

where $_{\text{geo}}$ relates to the geometric distance, $_{\text{tropo}}$ and $_{\text{iono}}$ to the atmospheric induced delays at the troposphere and ionosphere, respectively, $_{T-\text{clk}}$ and $_{R-\text{clk}}$ the transmitter and receiver clock offsets (note that the receiver offset cancels out, as both the direct and reflected signals are acquired with the same instrument at the same instant of time), $_{\text{instr}}$ accounts for other instrumental delays (cabling, connectors...), $_{\text{shape}}$ includes any delay error induced by unexpected distortion of the waveforms shape (sea surface roughness, sampling and filters, antenna pattern effects, near-field multipath, ...), and ϵ is noise. The altimetric information is embedded in the term $\Delta\rho_{\text{geo}}$

$$\Delta\rho_{\text{geo}} = |\vec{S}(\text{SSH}) - \vec{T}| + |\vec{R} - \vec{S}(\text{SSH})| - |\vec{R} - \vec{T}| \qquad (2)$$

being $\vec{T}$ and $\vec{R}$ the coordinates of the transmitter and receiver, respectively, and $\vec{S}$ those of the specular point on the sea surface, the latter depending on the SSH.

A common approach to extract $\Delta\rho_{\text{geo}}$ from the measured $\Delta\rho_{\text{LED}}$ is to correct for as many terms in (1) as possible (e.g.,

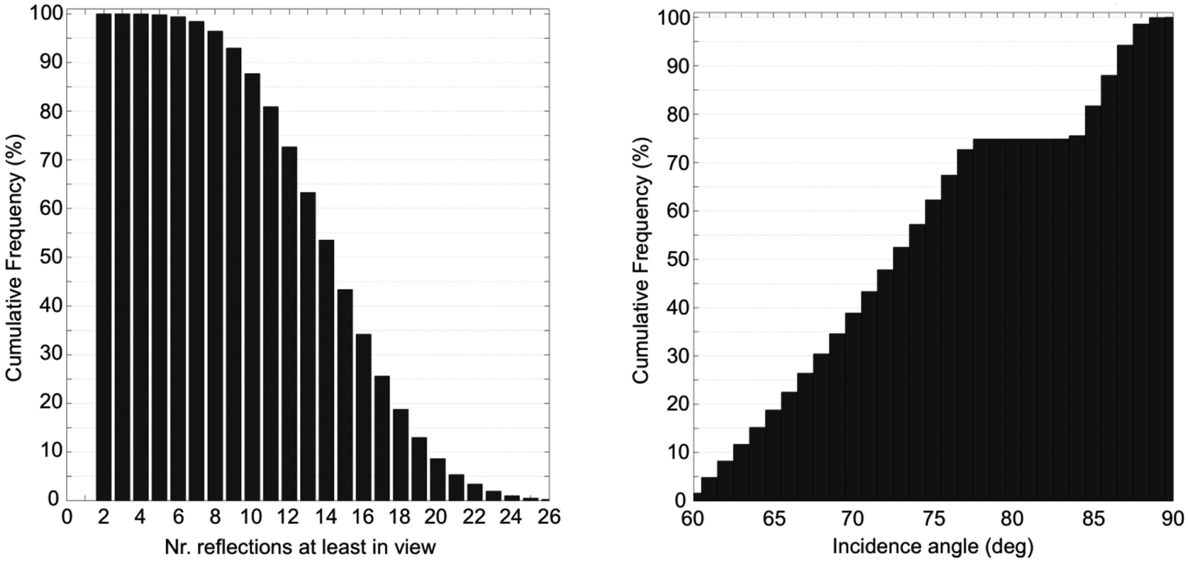

Fig. 13. GEROS FoV-2 cumulative distribution of the number of beams (left) and incidence angles (right).

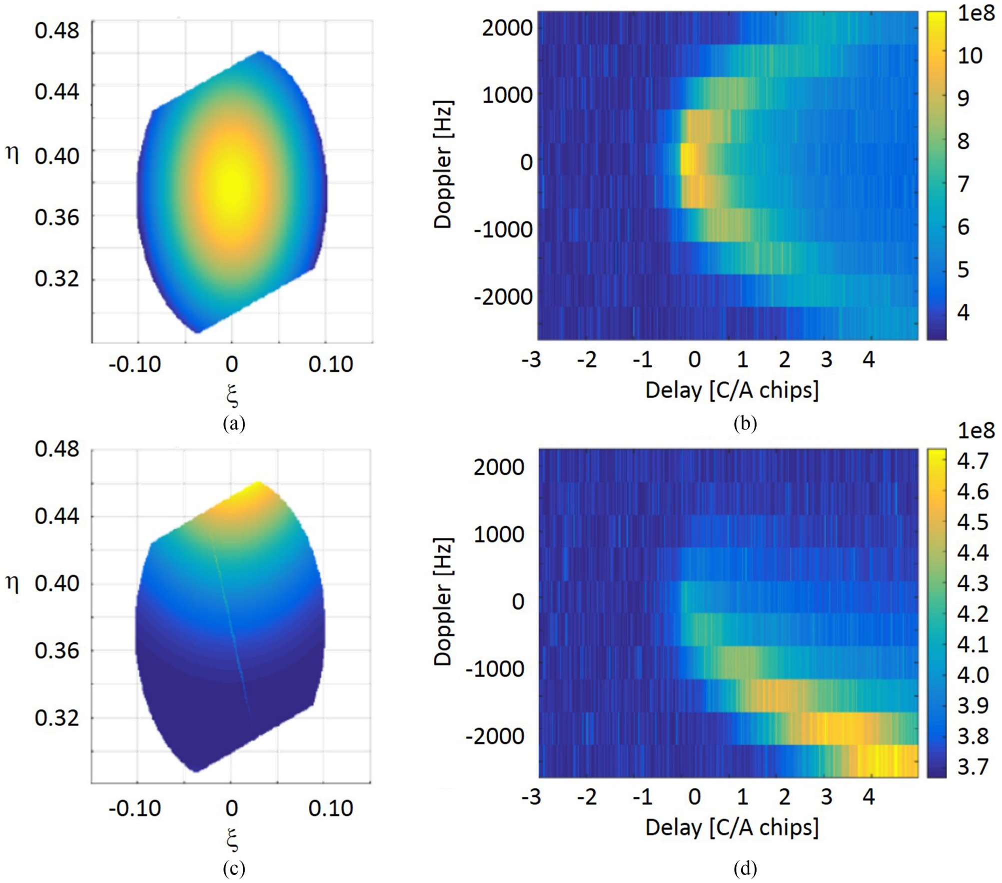

(a) (b)

(c) (d)

Fig. 14. Example of GEROS-SIM beam pointing simulation. A case of perfectly pointing to specular reflection: (a) antenna beam pattern (in direction cosine) and (b) corresponding DDM, and the case of 10 ° error: (c) antenna beam pattern, and (d) the corresponding DDM.

[35]). Most corrections rely on external information (atmospheric models or observations, International GNSS Service information, calibration of the receiver payload...). Any noncorrected or miscorrected term will be absorbed as $\Delta\rho_{\mathrm{geo}}$, introducing an error (bias or random-like) in the SSH retrieval. In GEROS-SIM, the approach taken is fully equivalent to these *a posteriori* corrections, but they are applied as input of a reference modeled waveform against which our observed waveform is compared. Any external available information is used to generate a modeled waveform that takes them all into account. The modeled waveform also uses a good *a priori* estimate of the SSH at the expected specular point location. Then the delay

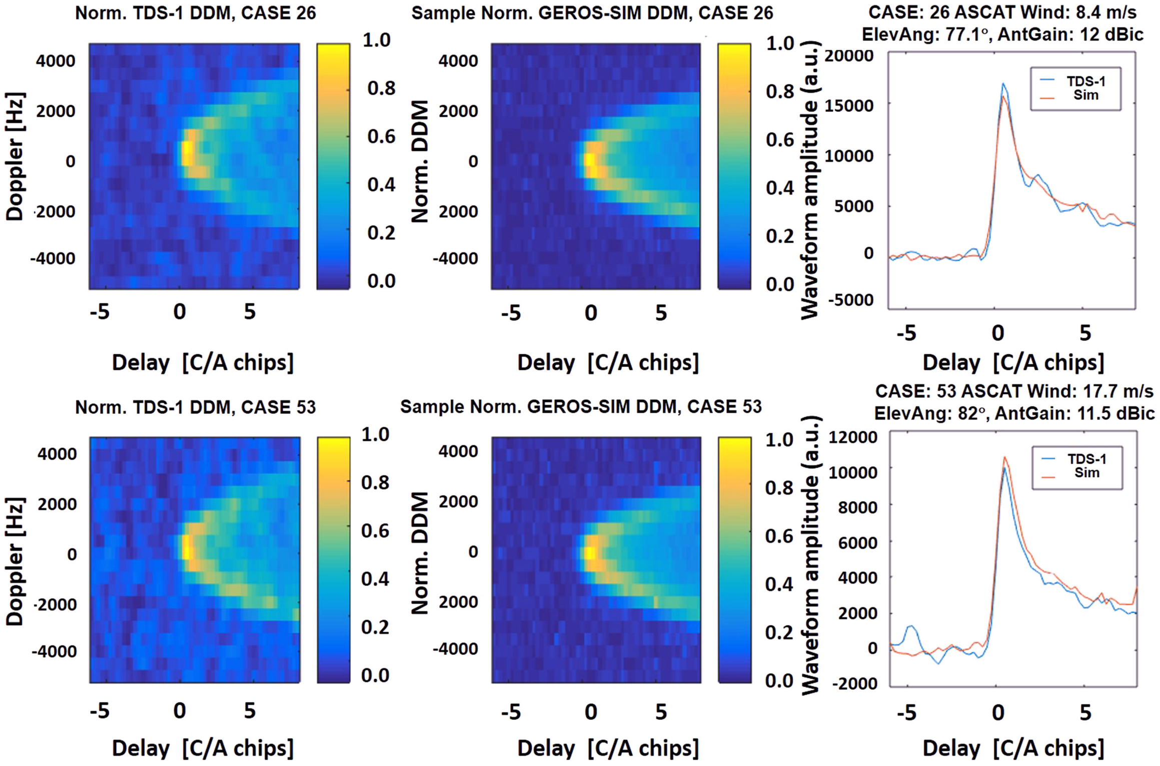

Fig. 15. Examples of GEROS-SIM validation test results comparing TDS-1 data. GEROS-SIM can generate waveforms in addition to the full and configurable—in terms of number of bins and spacing—DDMs.

of the peak of the LED is computed for both measured waveform, $\Delta\rho^{\mathrm{obs}}_{\mathrm{LED}}$, and modeled waveform, $\Delta\rho^{\mathrm{mod}}_{\mathrm{LED}}$. If the model were perfect both LED-delay would agree, meaning that the *a priori* SSH assumed in the model, SSH_0, was correct. If the *a priori* values were wrong, there would be a difference between the observed and modeled $\Delta\rho_{\mathrm{LED}}$, which shall be interpreted as a correction to the *a priori* SSH_0

$$\mathrm{SSH} = \mathrm{SSH}_0 + \frac{\Delta\rho^{\mathrm{obs}}_{\mathrm{LED}} - \Delta\rho^{\mathrm{mod}}_{\mathrm{LED}}}{2\cos\theta} \tag{3}$$

being θ the incidence angle at the specular point. If the model is accurate, this differential approach cancels out some of the distorting errors ($\Delta\rho_{\mathrm{shape}}$) as they are present in both actual data and model, such as surface roughness effects or well-characterized instrumental filters or sampling effects. Note that these type of distorting effects are harder to correct when using posteriori corrections for the systematic delay offsets (troposphere, ionosphere, clocks).

A study has been conducted to assess the impact of different mismodeling/miscorrections in the final altimetric retrievals, such as the errors introduced by the mistaken SSH_0 (how good the *a priori* must be?); residual effects of the troposphere and ionosphere; of the sea surface roughness; antenna pattern and pointing effects; errors induced by inaccurate orbit determination; or the effect of the speckle in the precision of the altimetric solution. The results agree with similar studies conducted for similar GNSS-R spaceborne altimetric missions, e.g., [23], [35], [37]. A brief summary is given below:

Errors in the *a priori* SSH_0 of a few meters would introduce cm-level inaccuracies in the SSH retrievals. This seems feasible taking into account the accurate knowledge of the mean sea surface topography and tide models. This LED-based and differential approach has also been shown to be robust to mismodeling of the sea surface roughness, introducing millimeter-level bias when simulations are run free of speckle and thermal noise. As for the tropospheric errors, we have considered that the corrections would be obtained from European Centre for Medium-Range Weather Forecasts (ECMWF) analysis products, which are not perfect. The error characterization of such products have been assessed using the dispersion and spatial correlation of ECMWF ensemble of data assimilation (EDA). The error characterization of the tropospheric fields has resulted in the values provided in Table II. Using these percentage errors and their spatial correlation, the systematic altimetric error produced by them is assessed using actual values of the ECMWF analysis fields, interpolated in time and space to the specular points of GEROS observations. Fig. 16 depicts an example of the tropospheric error in the altimetric retrievals generated for the OSSE exercise in Section V-B.3.

TABLE II
ASSESSMENT OF THE ERRORS IN ECMWF ANALYSIS FIELDS, AS OBTAINED FROM THE ANALYSIS OF ECMWF EDA PRODUCTS

Variable:	Percentage error:	Error correlation length:
Surface pressure:	0.03%	~500 km
Surface temperature:	0.16%	~400 km
Integrated water vapor (IWV):	(– 0.147 IWV + 8.457) %	~200 km

Errors in the antenna beam pointing smaller than ±5° introduce SSH errors smaller than 1 mm. Pointing errors smaller than these values seem feasible even from the ISS platform in

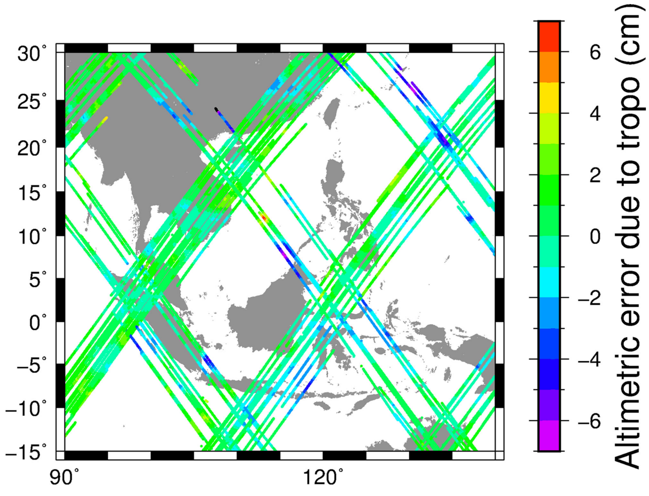

Fig. 16. Example of altimetric errors induced by the fact that the ECMWF analysis products are used as corrections of the tropospheric delay (term $\Delta\rho_{\text{tropo}}$) in (1), whereas these products do not represent the actual atmosphere, but mistaken as statistically indicated in Table II. The example corresponds to the area of the OSSE presented in Section V-B.3, as seen from FoV-1 for June 19, 2014.

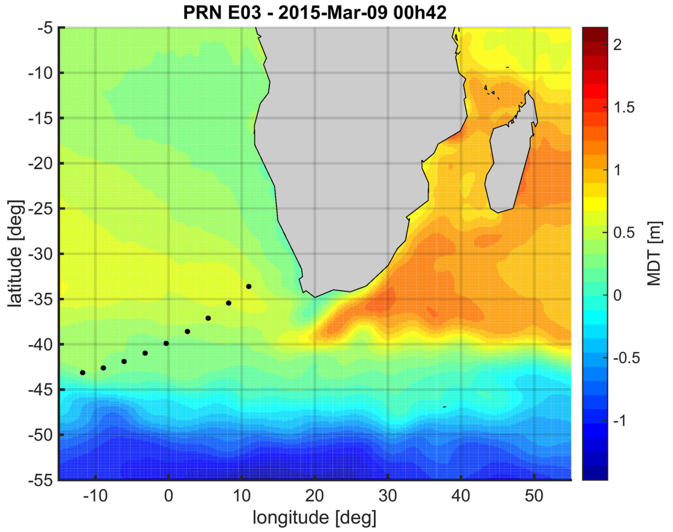

Fig. 17. Ground track of the E03 event (black dots) with 1 min time spacing. The Agulhas region is shown with the mean dynamic topography (MDT) of the sea surface, taken from the DTU-10 model.

most conditions. Errors in the radial component of the receiver positioning (POD) map directly as SSH errors. As a consequence, the radial component of the GEROS POD must have an accuracy within the GEROS altimetric objective. This seems feasible as discussed in Section IV-D.

Errors in the assumed ionosphere of the order of 1 TECU introduce large errors in both L1 and L5 altimetric solutions (a few decimeter level), but they are strongly reduced when using the ionospheric-free combination (e.g., [38]) applied to the single-frequency SSH solutions. This results in unbiased solutions when using simulated data free of speckle, thermal noise, and ionospheric scintillation effects. Nevertheless, specke-free data is unrealistic and it is well known that ionospheric-free frequency combinations further increase the noise of the solution.

Among all the effects evaluated in this study, the noise associated to the speckle has the largest contribution to the random-component of the precision budget. The effect is a random dispersion of the SSH retrievals, with a standard deviation below 0.5 m for observations at 1 s integration (GPS L1 with smoothed 2-frequency ionospheric correction). Together with the rest of the precision figures assessed in this study [18], this finally represents less than 15 cm in 100 km averaging, which fulfills the objectives of the mission. This level of precision agrees with the analyzes of similar GNSS-R scenarios in [23], [35], [39] and it is consistent with the CRB analysis performed for the mission (see Fig. 9). Moreover, as shown in [40], the precision could still be improved by multi-Doppler processing techniques.

2) Phase Altimetry: The motivation of phase delay altimetry lies in the centimeter precision of GNSS phase observations to be used for sea surface anomaly measurements. The resolution of such decimeter scale anomalies on a submesoscale (in time and space) is still challenging [41]. Investigations to improve resolution by potential phase altimetric observations are important in this respect. The altimetric use of GNSS-R carrier phase information has been demonstrated already over the Antarctic ice sheet based on spaceborne records [42], over in-land lakes [43] and over the Mediterranean sea [21] based on airborne records in the range of elevation angles between 0° and 30°, respectively. Geometries closer to the nadir generally cannot provide continuous phases, as the surface roughness increases the diffuse component of the scattering. Phase delay altimetry for ISS therefore is constrained to FoV-2.

Simulation results for an ISS-based receiver setup are presented here. A comprehensive description of the phase altimetric simulator and aspects of potential observations made on a low earth orbit are found in [44]. The following simulation demonstrates the retrieval of ocean topography signatures based on phase residuals. The presented case study assumes sufficient correction of troposphere and ionosphere effects. An *a priori* sea surface given by the geoid is considered. This means that only the ocean topography $h = H - G$ remains for simulated retrieval where H denotes the ellipsoidal SSH and G is the surface undulation w.r.t. the ellipsoid that is provided by geoid models [45], [46]. The retrieval concept, based on topography-dependent phase residuals $\phi(h)$, has been demonstrated experimentally for airborne records cf. [21]. In the following part, a simulated reflection event over the Agulhas current region is considered, see Fig. 17, as a potential example of spaceborne records.

It belongs to the Galileo satellite PRN E03 observed at the ISS on March 9, 2015 00:43 UTC and comprises 9 min of simulated observations. The satellite passes elevation angles between 5° and 30° long the 2500 km reflection track. These angles are observed at the reflection points and correspond exactly to the GEROS FoV-2 with 54–66° nadir angle at the ISS. The mean dynamic topography (MDT) model [47] rises from about 30 to about 60 cm with respect to the geoid along this track.

Height Retrieval: A comprehensive description of the height retrieval is given in [44]. The following simulation concentrates on the topography resolution and the ambiguity effect within the phase altimetric retrieval. Noise-affected phase data are simulated based on MDT information and plotted in

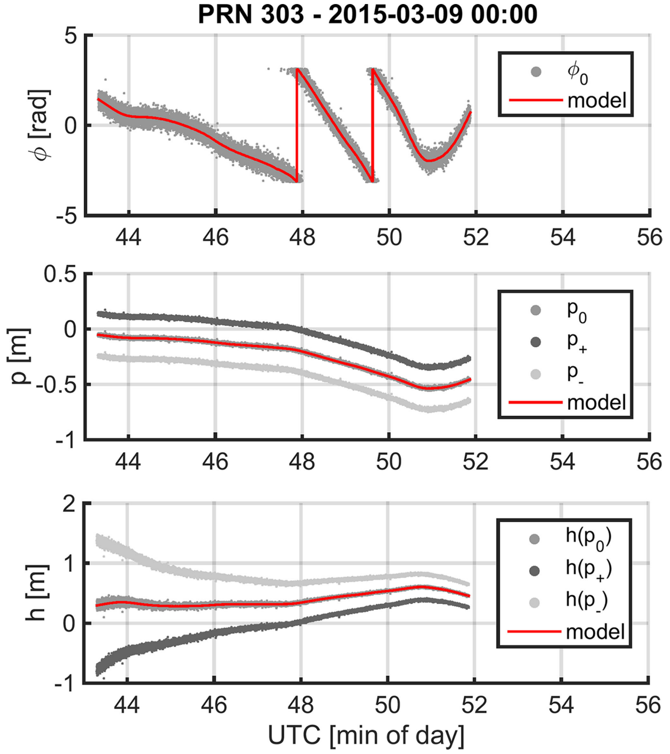

Fig. 18. Phase altimetric retrieval in three panels starting from phase residuals ϕ via phase path estimates p resulting altimetric tracks h. MDT-based model information (red line) is added in each panel. There is a model compliant estimate p_0 (gray). Two further estimates p_+ (dark gray) and p_- (light gray) are shown with deviating ambiguity solutions. Different tracks h result from p_+, p_0, p_-.

Fig. 18 (first panel). The wrapped phase ϕ shows aliasing in the range $(-\pi, +\pi)$ and does not necessarily map the complete topographic information. The aliasing effect is corrected by an unwrap operation U (MATLAB standard algorithm) adding $\pm 2\pi$ if changes $|\Delta\phi| \geq \pi$ occur (unwrap condition). Furthermore, the resolution of the integer ambiguity N is required to construct a path estimate that finally reads

$$p = \lambda \left[\frac{U\{\phi\}}{2\pi} + N\right] \tag{4}$$

depending on the GNSS carrier wavelength λ. The second panel shows three ambiguity solutions p_+, p_0, p_- for respective N being $+1$, 0, -1. The model-compliant ambiguity solution is trivial ($N = 0$) as the initial path residual is smaller than the wavelength. A phase ambiguity solution is not required in this case. These estimates can be mapped to altimetric results

$$h = \frac{p}{2 \sin E} \tag{5}$$

where E denotes the transmitter elevation angle defined in the reflection point. The results are plotted in the third panel of Fig. 18. According to the path estimate, the track $h(p_0)$ shows best agreement with the underlying MDT model. Tracks for the other solutions $h(p_-)$ and $h(p_+)$ have a significant deviation from the model (starting with several decimeter). The decrease in deviation magnitude is remarkable. It is related to the increase of E from 5° to 30° during the event and has two consequences. On one hand, it indicates the increase of altimetric precision with elevation. On the other hand, it shows that the ambiguity solution is easiest at low elevation angles where the separation of possible solutions N is particularly large. Scenarios of residual troposphere and ionosphere effects and the influence of the SNR on the height retrieval are examined in [44]. Furthermore, ocean roughness influences the retrieval and is a critical parameter with respect to a sufficient SNR [48].

The simulated event, considered here, has a rather small topography range. The concept also applies for larger ocean topography variations that occur, for example, in the eastern Agulhas region, cf. Fig. 17. In general, it applies at rather low elevation angles (here assumed from about 5° to 30°) as solutions N are then more easily confined and as the impact of ocean roughness is reduced there. Phase altimetry at these elevations potentially improves the coverage achieved with code altimetric observations (with $E > 60°$).

3) Scatterometry: By virtue of its passive nature and the potential for multiple simultaneous measurements across a wide swath, GNSS-R offers attractive possibilities also to improve global monitoring of ocean surface winds. These measurements belong to the second main mission objective of GEROS. It is foreseen to provide scalar ocean surface MSS, which is related to sea roughness, wind speed and direction.

The feasibility of spaceborne GNSS-R for scatterometry was first demonstrated and validated by the pioneering GNSS-R experiment by Surrey Satellite Technology Ltd (SSTL) onboard the UK-Disaster Monitoring Constellation satellite in 2003. At that time, only about 50 separate data acquisitions were performed over the ocean ([49], [50]), with just a handful of data ever becoming available to the wider community for analysis ([51], [52]). This shortage of spaceborne GNSS-R data was finally addressed following the successful launch by SSTL on July 8, 2014 of the UK-funded TDS-1 satellite and its GNSS-R Sea State Payload (SSP) instrument. Since then, efforts have been underway at the National Oceanography Centre (NOC) and SSTL to develop and publicly disseminate TDS-1 SSP Level 1 DDM and Level 2 wind speed products via the web-based MERRBys portal (http://www.merrbys.co.uk). NOC is also responsible for the development of the GEROS "Level 1 to Level 2 Processor" for the surface winds, which profited significantly from the availability of real satellite data from TDS-1.

Level 2 Wind Speed Inversion Algorithms: So far, two types of Level 2 wind speed inversion algorithms have been investigated at NOC: the so-called "Fast-Delivery Inversion" algorithm (FDI) and the more complex "Bistatic Radar Equation" algorithm (BRE). Both algorithms are based on the SNR calculated as the ratio of the average signal power (S) in a box located around the peak of the DDM and the average noise power (N) measured in a noise box in the signal-free area. For both algorithms, the size of the signal box is chosen to achieve a spatial resolution around 25 km. For TDS-1, the dimensions of the signal box are 1 chip (4 delay bins) by 1500 Hz (3 Doppler bins) corresponding to a spatial resolution between 22 and 30 km (median value 25 km) depending on the elevation angle of the specular point. Since the position of the peak can fluctuate in both delay and Doppler space, the signal box is positioned dynamically around the peak using an automatic peak detection scheme based on the application of a median filter and extraction of the local maxima in the DDM.

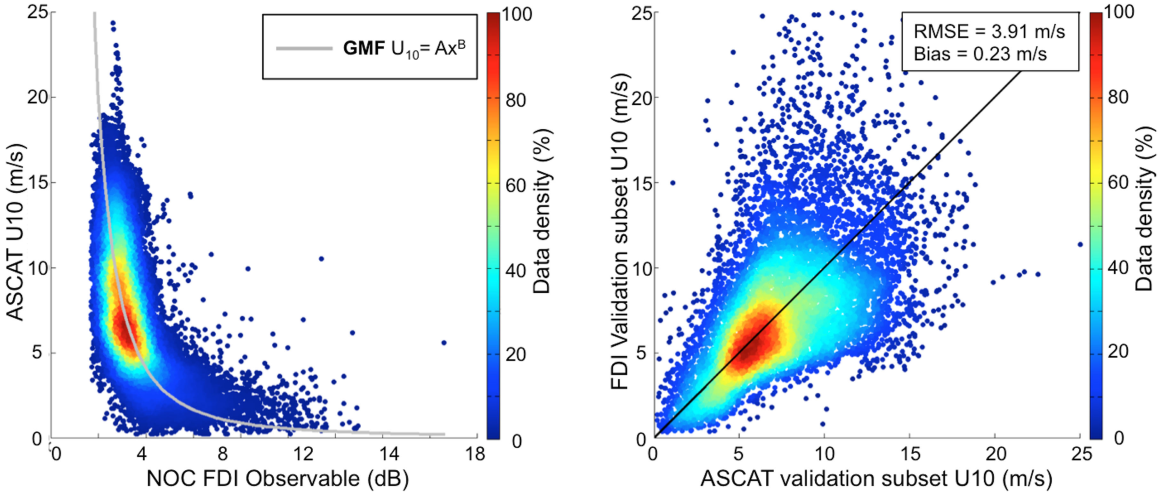

Fig. 19. NOC (National Oceanographic Centre) fast-delivery inversion algorithm for TDS-1: Left—Two-dimensional histogram of the TDS-1/ASCAT matchup dataset and fitted empirical power law relating U10 to SNR; Right—Retrieved TDS-1 wind speed against ASCAT winds for a validation subset of the TDS-1/ASCAT matchup database.

The BRE algorithm is an advanced inversion model that corrects for the GNSS-R bistatic viewing geometry and the receiver antenna gain pattern effects in accordance with the BRE. A full description of the BRE algorithm and its performance can be found in [11]. Briefly, [11] showed that TDS-1 BRE wind speed are retrieved without bias and a precision around 2.2 m/s for winds between 3 and 18 m/s, even without calibration.

In contrast, the FDI algorithm is a simple empirically based inversion developed from spaceborne GNSS-R measurements acquired with TDS-1 while operating in automatic gain mode. The only essential inputs to FDI are the SNR from the Level 1 DDMs and the antenna gain at the specular point (AGSP). The FDI was designed as a placeholder for the MERRBys portal to rapidly deliver TDS-1 Level 2 wind speed products in a simple easy-to-understand format for potential operational and commercial end-users of the data. The aim of FDI was, therefore, not to achieve the best possible retrieval performance, but to quickly deliver Level 2 product that demonstrate the sampling capability of GNSS-R and encourage the uptake of GNSS-R data by users.

The FDI algorithm was derived from a globally distributed matchup dataset of TDS-1 GNSS-R data collocated with surface wind speed from the METOP ASCAT-A/B satellite scatterometers. ASCAT data were collocated within 1 h and 1° of latitude/longitude of TDS-1 and correspond to 10 m wind speed over ice-free and rain-free ocean conditions. The matchup dataset served to establish the empirical relationship between SNR and surface wind speed, which is illustrated in Fig. 19. The relation can be approximated by a power law with fitted coefficients determined by least-square fitting of the TDS-1 data

$$U_{10} = AX^B, \tag{6}$$

and

$$X = SNR - k_1 * AGSP + k_2. \tag{7}$$

Nominal values of A, B, k_1 and k_2 for TDS-1 are 97.24, −2.28, 0.215, and 3, respectively.

Application to GEROS: Validation of GEROS-SIM for Scatterometry: The “L1-to-L2-Processor-Scatterometry” module of GEROS-SIM (see Fig. 10) is based on the implementation of the NOC FDI algorithm developed for TDS-1. A series of tests was performed to validate the GEROS-SIM simulation suite in its integrated form, consisting of the application of the processing module to 1 Hz DDM produced by the GEROS-SIM Instrument-to-L1 module.

The complete simulation suite, beginning from Level 0 instrument data was tested for several instrument configurations, including one that adopted parameters representing as closely as possible the mission characteristics of TDS-1 in terms of altitude, antenna-beam pattern/pointing, DDM size/resolution, etc. The TDS-1 setup consists of a fixed highly directional receiving antenna with main beam pointing slightly off-nadir (6° behind the spacecraft in the direction of flight), so that changes in incidence angle at the specular point are also associated with changes in AGSP. GEROS-SIM was also tested for setup parameters representative of the GEROS instrument and orbital elements of the ISS platform. However, only results for the “TDS-1 setup” are presented here.

The input test parameter space for the simulations comprised a wide range of wind speeds and incidence angles. The parameters used to run GEROS-SIM in the “TDS-1 configuration” are summarized in Table III. The incidence angle at the specular point ranged from 0° (nadir) to 60° in 10° steps. In order to avoid possible numerical singularities, the incidence angle at nadir was deliberately set to 0.01°. Retrieved wind speed resolution will vary according to the size of the illuminated surface area corresponding to the fixed-size DDM signal box selected by the scatterometry algorithm. Illuminated area depends on the incidence angle following an inverse cosine-square law $1/\cos^2\theta$, where θ is the incidence angle.

Input U10 spanned across three wind speed regimes—low, medium, and high winds—with different incremental steps, which overall covered the range 0.01 to 60 m/s wind speed. This permitted detailed assessment of the performance of the integrated GEROS-SIM across the full range of wind speed

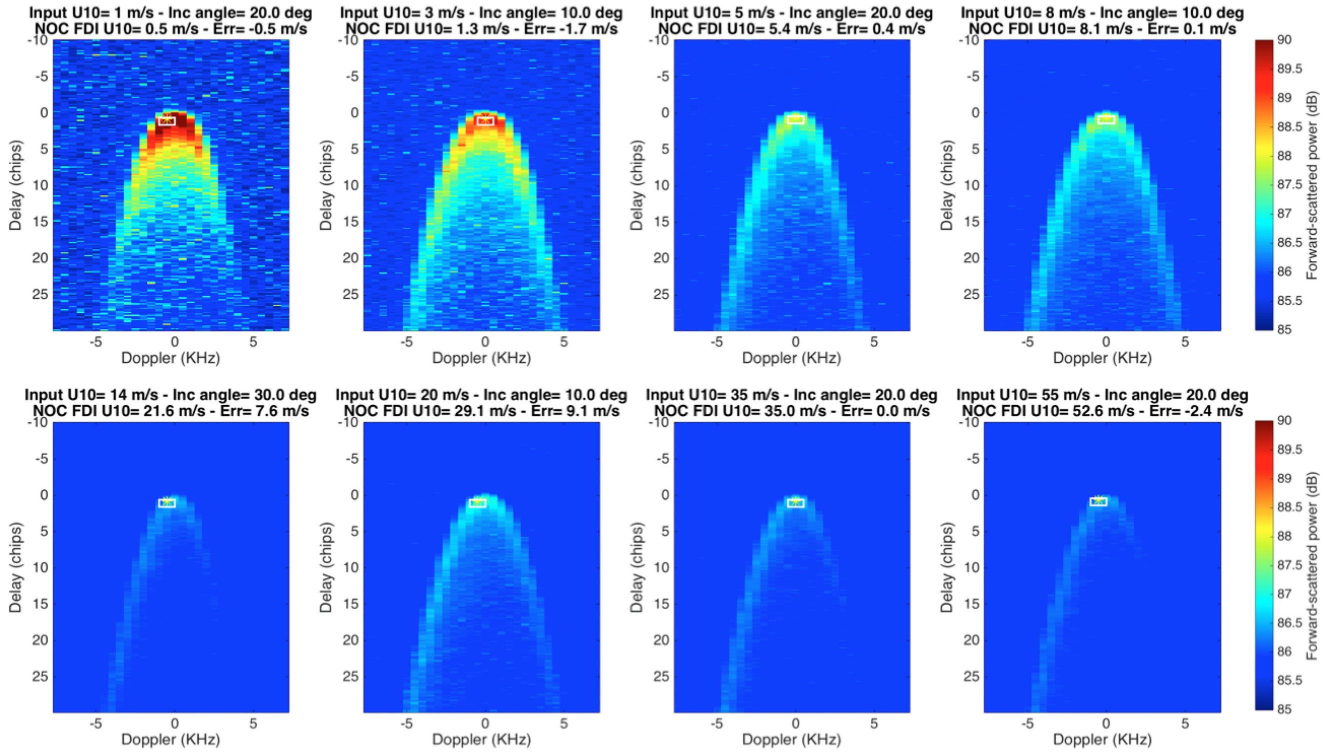

Fig. 20. Examples of L1 DDM produced by the GEROS-SIM M2 module with the TDS-1 configuration. The L1 DDM correspond to different wind speeds and incidence angles as indicated in the legend of each subplot (Inc: 0.1° corresponds to nadir).

TABLE III
PARAMETERS OF THE GEROS-SIM SIMULATOR IN THE TDS-1 CONFIGURATION

Receiver altitude	635 km
Coherent integration time	1 ms
Incoherent integration time	1 s
Number of delay bins in DDM	200
Delay bin resolution	0.2 C/A chip
Number of Doppler bins in DDM	30
Doppler bin resolution	500 Hz
Maximum antenna gain	13.3 dBi
Incidence angle at the specular point	0.01 (near-nadir), 10, 20, 30, 40, 50, 60 deg
Input wind speed	Low range: 0.01, 0.05, 0.1, 0.25, 0.5, 1, 2, 3 m/s Medium range: 3–20 m/s (3 m/s interval) High range: 20–60 m/s (5 m/s interval)

regimes. However, the current implementation of the GEROS-SIM simulator solely supports spatially uniform winds across the glistening zone. This is not always fully representative of reality, particularly so at high ($U_{10} > 30$ m/s) wind speeds.

Examples DDMs produced by the GEROS-SIM Instrument-to-L1 processing module are shown in Fig. 20 for a subset of the input wind speed and incidence angles detailed in Table III. The format and appearance of the simulated DDMs were found to be qualitatively consistent with real DDM measured with TDS-1.

Next, the Scatterometry module was applied to the L1 dataset produced by the Instrument-to-L1 module for the full range of parameters shown in Table III, corresponding to approximately 150 individual simulations. Fig. 21 shows the SNR estimated with the NOC FDI algorithm of the L1-to-L2-module against input wind speed. The simulated SNR was found to decrease with increasing input wind speed, with the sensitivity to wind speed asymptotically tending to zero at high winds. In this TDS-1 configuration, the SNR also decreases with increasing incidence angle, which agrees with experimental observations from TDS-1.

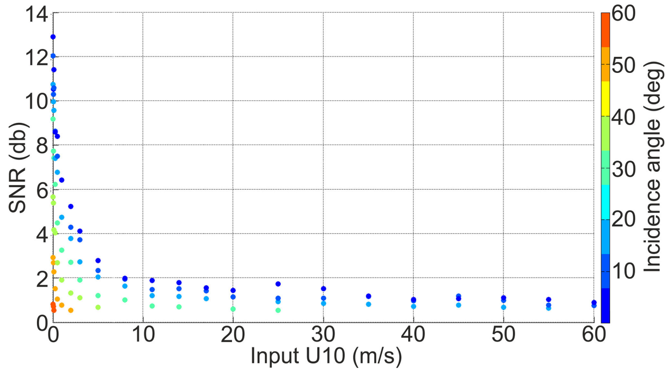

Fig. 21. Signal-to-noise ratio obtained with the GEROS-SIM M5 scatterometry module applied to M2 L1 DDM obtained for different input wind speed and incidence angle of the specular point (Inc: 0.1° corresponds to nadir).

Finally, the FDI algorithm was tuned to the GEROS-SIM simulated data to obtain the fitted parameters of the FDI geophysical model function for GEROS-SIM. Given the limited number of simulator realizations available (96), the training dataset was also used for validation. The results are shown in Fig. 22. After tuning, the performance of the simulated L2 wind speed for GEROS-SIM was found to be similar to that obtained with

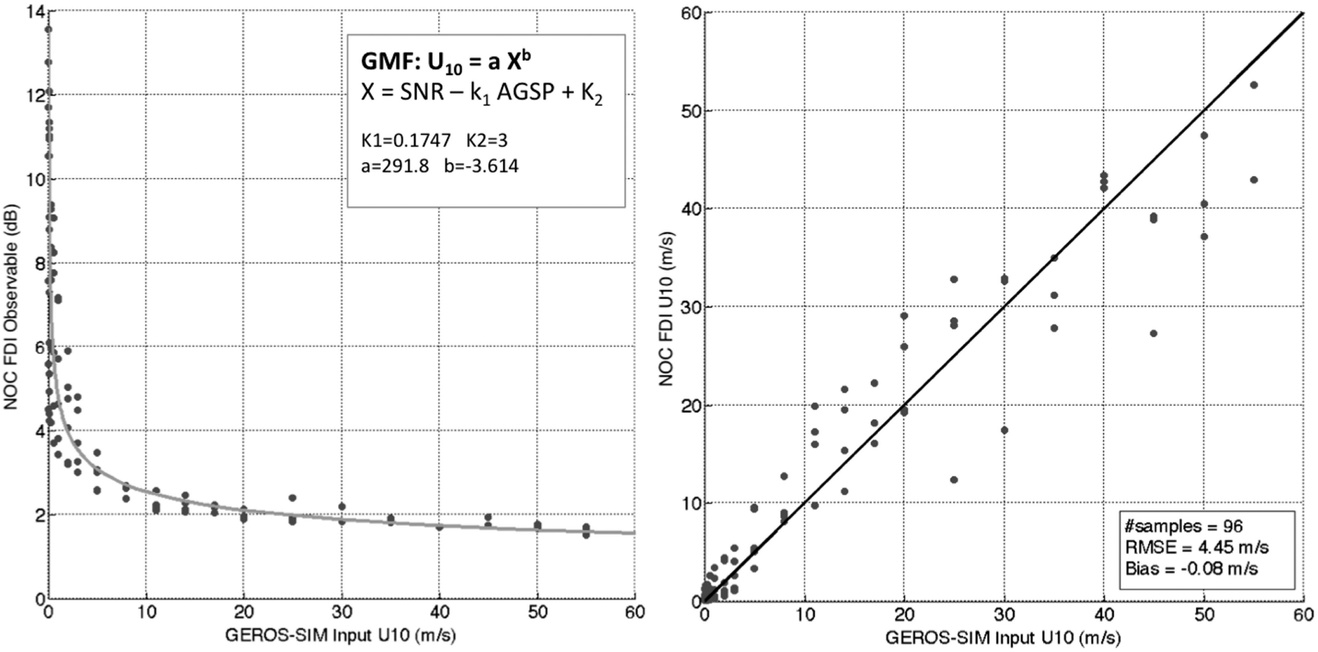

Fig. 22. GEROS-SIM results with the TDS-1 setup showing (left) the FDI algorithm tuned to GEROS-SIM data and (right) the performance of the retrieved L2 wind speed for GEROS-SIM.

TDS-1 data, namely wind speed is retrieved with very small bias and with a precision around 4.5 m/s in the 0–60 m/s wind speed range and across all incidence angles. Although further tests are needed to fully validate the GEROS-SIM simulator for scatterometry, these preliminary results give confidence in the ability of GEROS-SIM to realistically capture the main characteristics of GNSS-R signals over the ocean.

D. Precise Orbit Determination for GEROS

The success of the GEROS experiment critically depends on the ability to accurately geolocate the phase centre position of the GNSS-R antenna in a well-defined Earth-fixed terrestrial reference frame. For this purpose, POD using GNSS carrier phase tracking data, collected by a dedicated zenith-looking antenna, is a prerequisite and thus a key task of the GEROS experiment. Most stringent POD accuracy requirements are needed for many satellite missions, typically demanding (1-D) position RMS errors of few centimeters, e.g., for gravity missions such as GOCE [53] and altimetry missions such as Jason-2 [54]. Especially the radial component is crucial for the altimetry missions to derive high quality data products. We note that the POD measurements from GEROS also can be used for three-dimensional (3-D) upside ionosphere monitoring, as initially demonstrated with data from the CHAllenging Minisatellite Payload [55] satellite [56]. Offline reduced-dynamic POD based on dual-frequency GPS data has been evolved to a mature and well-established technique offering cm-accuracies, provided that the attitude motion of the onboard GNSS receiver antennas in inertial space is precisely known from additional measurements, e.g., star camera readings, and/or using additional GNSS antennas. Only marginally worse accuracies are today achieved in the kinematic mode if the number of simultaneously and continuously tracked GPS satellites is sufficiently large [57]. Whereas reduced-dynamic POD of the center-of-mass position of a smaller satellite is in principle straightforward, a much greater challenge is posed by large platforms such as the ISS [58]. Significant errors might be introduced by the inaccurate knowledge of the center-of-mass position with respect to the POD antenna phase center, the poor knowledge of deformations and vibrations of the platform structure, for example, due to Earth shadowing effects, and the presence of signal obstruction effects degrading the number of simultaneously tracked satellites even for zenith-looking POD antennas. Even when using dual-frequency GNSS data, the achievement of subdecimeter orbit accuracies for the ISS would be a challenge when relying on dynamic POD. Due to these difficulties, a kinematic determination of the phase center position of the POD antenna is planned for the GEROS experiment. For this purpose, the POD antenna is embedded as part of the GEROS antenna itself, removing the need for auxiliary attitude knowledge of the ISS. With a typical separation of 10–20 cm between the up-looking and down-looking antenna, an attitude uncertainty of the ISS of about 3°–4° only translates into a vertical impact of about 0.3 mm in the worst case.

E. GNSS Radio Occultation with GEROS

A further additional objective, which was identified already in the GEROS proposal is GNSS-based RO for precise sounding of the neutral atmosphere and the ionosphere. GNSS-RO data are currently already operationally available from several missions, e.g., FORMOSAT-3/COSMIC, Metop-A/B, GRACE, or TerraSAR-X [59], [60] and several new operational missions with GNSS-RO will be realized (e.g., COSMIC-2, EUMETSAT Polar System—Second generation, EPS-SG). Therefore, the need to get RO data from GEROS is less compelling and is regarded as mission goal with lower priority, compared to GNSS-based ocean remote sensing.

TABLE IV
LIST OF FORESEEN DATA PRODUCTS FROM GEROS

Sea Surface Height:
L1: Time collocated waveforms of the reflected signals
L2: Sea surface height along the reflection tracks, geo-located and time-tagged
Mean Square Slope:
L1: Waveforms or Doppler Delay Maps of the reflected signal
L2: Surface roughness, wind speed, geo-located and time-tagged
Precise Orbit Determination:
L1: Dual frequency GNSS POD data, GNSS-R antennae phase centers
L2: POD and GNSS-R antennae phase centers, inter-constellation bias data
GNSS Radio Occultation:
L1: Dual frequency excess phases, bending angles
Scatterometry over land (if instrument allows):
L1: Time collocated waveforms or Doppler Delay Maps of the reflected signals

Nevertheless, there are several new aspects supporting RO measurements within GEROS. These are as follows:

1) Innovation for the RO technique: The ISS inclination allows for better data coverage and stronger RO signals in the tropics and the mid-latitude regions compared to the polar/near-polar orbiting RO missions. GEROS might enable initial application of Galileo and GLONASS signals for RO, as well as initial application of the polarimetric occultation concept for the detection of strong precipitation events [61], [62] in parallel and to continue measurements of the Spanish PAZ satellite.
2) Strong complementarity to the GNSS-R approach, the coherent reflectometry measurements for altimetric measurements of sea and ice surface topography (part of the primary mission goal, [42], [63]).
3) Provision of useful additional atmospheric (dry and wet tropospheric) and ionospheric delay information partially collocated with the GEROS GNSS-R measurements and relevant for the analysis and correction of the reflectometry measurements for ocean surface height measurements obtained aboard ISS.
4) Application of a new interferometric RO technique [64]. This approach replaces the use of the on-board generated code replicas by recorded segments of the live received GNSS signals. The GEROS payload, designed for best altimetry performance, enables such kind of RO processing in a rather straightforward manner.

F. Anticipated GEROS Data Products

The GEROS mission foresees the classical Level 0 to Level 2 data product generation chain. Level 2 products will be the main products for the geophysical user community. Additional products and higher level products (Level 3) are expected to be derived by scientific institutions and national groups interested in the GEROS data. Table IV overviews the potential data products.

The GEROS data products will be made available and archived for the international scientific user community via one or several specialized GEROS scientific data processing and archiving centres. A broad scientific and interdisciplinary GEROS user community will be formed by regularly data user workshops, by joint scientific investigations resulting in publications in leading international geoscience journals and by joint acquisition of third party funded research projects to support the scientific exploitation of the GEROS data.

GEROS products could contribute to the global database for operational weather and oceanic forecast systems. A precondition for this purpose is a near-real-time provision of the data products (e.g., 3 h after the measurement for meteorological data), which requires additional specific mission infrastructure elements. Since GEROS is an experimental and demonstration mission, such full operational data product provision is not foreseen in the current mission state but is planned to be demonstrated within dedicated experiments for near-real-time product provision.

V. SCIENTIFIC STUDIES

Part of the preparation of the GEROS mission and the work of the SAG are dedicated scientific studies and campaigns, which are summarized here.

A. Baltic Flight Campaign

The interferometric GNSS-R approach suggested at this stage of the GEROS mission was experimentally proven and reported in [65] (ground-based experiment) and [35] (airborne experiment). The technical feasibility and the altimetric performance of such technique were both explored in these campaigns, but using a simple single-beam high-gain antenna without any possibility to test the synoptic capabilities (wide swath) of the concept. Given that the iGNSS-R technique cannot separate the source of signal by code demodulation techniques, it must be done by antenna footprint discrimination from different and simultaneous beams of the antenna. Hence, the receiving system must enable simultaneous multiple beam-forming and pointing capabilities. An iGNSS-R instrument of this type did not exist and it had to be developed for such testing exercise. The Software PARIS Interferometric Receiver (SPIR) is a very high rate data logger that includes two antenna arrays, one looking upward and the other looking downward, of eight elements each. The signals collected by each one of the sixteen antenna elements are down-converted and their 1-bit quantized in-phase and quadrature components sampled at 80 MHz. This generates a stream of data of 2.5 Gbit/s (320 MBytes/s) sustained during several hours, typical length of airborne experiments. The signals from each antenna element are synchronized through a common clock and time-tagged by a commercial GNSS receiver chip. This recording approach enables to test any processing strategy (iGNSS-R and others), from as many simultaneous visible sources (elevation range given by the antenna pattern of a single antenna element, of ∼7 dB directivity each).

An airborne campaign was conducted in May 2015 over the Baltic Sea, following a similar trajectory as in 2011 iGNSS-R demonstration campaign [35]. Despite RF interferences generated by the prototyped instrument, the analysis of the data has permitted to confirm (and slightly improve) the altimetric precision obtained in the simple single-beam instrument in 2011 experiment. Agreement was found in both the single observation precision (∼0.15 m in 10 s integration in 2015 versus ∼0.19 m in 2011), as well as the ratio between the clean-replica

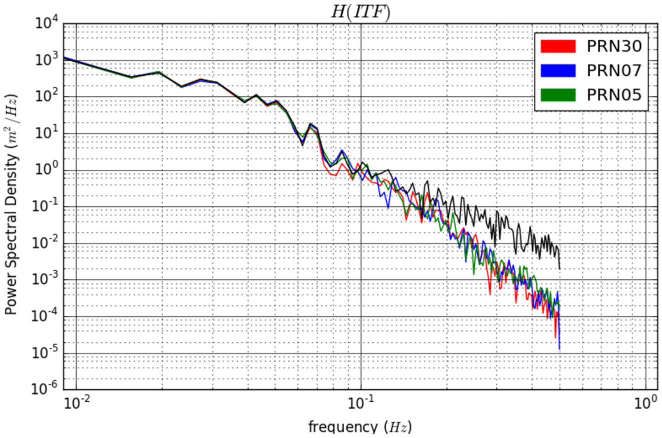

Fig. 23. Power spectral density of the recovered aircraft trajectory (black line), and three iGNSS-R solutions from three GPS sources: (red) PRN30 at incidence angles between 76°–79°, (blue) PRN07 at incidence angles between 55°–61°, and (green) PRN05 between 47°–49° incidence angles. The mean solution has been removed before analyzing the PSD.

and interferometric approaches (1.4 to 1.7 in 2015, depending on the GNSS source, versus 1.87 in 2011—one single GNSS source). Problems to precisely retrieve the aircraft trajectory (driven by the interferences generated by SPIR hardware) hindered the obtention of a final absolute altimetric solution. However, as illustrated in Fig. 23, the power spectral density (PSD) of the retrieved solutions are driven by the trajectory fluctuations in those features longer than 10 s. Furthermore, there is agreement between the PSD of the three altimetric solutions, and all present lower noise levels than the trajectory at time scales shorter than 10 s.

B. Observation System Simulation Experiments

OSSEs have been widely used to evaluate potential impacts of future observations [66], [67], in particular, those from new satellite sensors in modeling and predicting environmental phenomena. In OSSEs, the "truth" state is generated by a so-called "nature run" or "nature simulation"using a comprehensive and realistic model. Synthetic "observations" are acquired directly from the "nature run" (or from a retrieval algorithm of a specific measurement) using the sampling characteristics of the target observing system. The corresponding measurement errors are simulated and added to the synthetic observations. A different model run (called the "control run") is then performed with different initial conditions and/or model forcing/parameters so that the model state is different from the "nature run." The synthetic observations are assimilated into the control run. The impact of the synthetic observations is examined by assessing how well the assimilation run reproduces the true state.

Several OSSE were conducted to investigate the potential of the GEROS data to improve oceanographic forecast capability. We briefly review the three studies, performed by GFZ, JPL, and NERSC.

1) JPL: The OSSE studies from JPL have focused on the potential of GNSS-R altimetry on detection and representation of mesoscale ocean features, such as eddies, filaments, and fronts. One study is to assess the impact of GNSS-R SSHs in the model analysis and forecast of the shedding of a loop current eddy in the Gulf of Mexico during 2011 using OSSEs. The shedding of loop current eddies has major impacts in the physical, biological, and chemical conditions in the region. However, its prediction remains a challenge.

At JPL, a variety of OSSEs have been conducted and analyzed, employing a multiscale 3-D variational data assimilation system [68]–[70]. The measurement errors in SSHs are specified to have a Gaussian distribution and a mean error of 0.5 m for normal incidence angle (the nadir point). The mean error is specified conservatively and stems from a realistic assumption for the GEROS antenna gain, and the preliminary knowledge of the link budget. Since the delay, bending, and other errors proportionally depend on the incidence angle, this dependence is taken into account by a factor of $1/\cos\theta$, where θ is the incidence angle of the transmitter with respect to normal. Because of the dependence on the incidence angle, only those observations with an incidence angle less than 60° are used. In this case, the footprint size can be approximately specified as 10 km [71]. Synthetic SSH observations derived from the nature simulation are assimilated every 12 h.

There was an eddy shedding event in November 2011. The model simulation that is used as the true state realistically reproduces the shedding event. The model with the assimilation of the SSHs from the ISS receiver recovers the shedding event, although the shedding eddy is weaker (0.3 m in amplitude) than the one in the true state (0.5 m in amplitude, Fig. 24). In contrast, the model without data assimilation (control run) reproduces the shedding eddy event with 0.2 m in amplitude. These OSSEs indicate the potential of enhancing the model capability of representing the eddy shedding using the ISS GNSS-R SSHs.

Recently, further analysis at JPL has shown that mesoscale SSH fields can be mapped down to a scale of 100 km for two days [71], assuming that there are six receivers on board of six high-inclination satellites such as those of the COSMIC-2 (http://www.cosmic.ucar.edu/cosmic2). The assimilation of SSHs from these six receivers accurately reproduces the eddy shedding (see Fig. 24). This result highlights the potential of increase in the impact of the ISS GNSS-R SSHs when they are combined with other GNSS-R SSHs from possible future missions.

Another important implication of these OSSEs is that the modeling and data assimilation system is able to effectively digest the GNSS-R SSHs, although the measurement errors range from 0.5 to 1.0 m. Such measurement errors are two orders of magnitude larger than the measurement error of the traditional nadir altimetry. The tolerance of a model and data assimilation system to the large GNSS-R errors arises from its high spatiotemporal density. The high observation density allows the data assimilation process to smooth the measurement error down.

2) GFZ: The GFZ conducted an OSSE that studied and compared the performance of different GNSS-R measurement configurations [72]. The configurations differ in the assumptions about the observations precision (code or phase precision) and in assumptions about the usable range of reflection angles. The latter assumption is closely linked to the expected spatiotemporal density of the observations. Respective observations of SSH are simulated for the ocean current system around the South African coast. The noisy observations and their precisions are

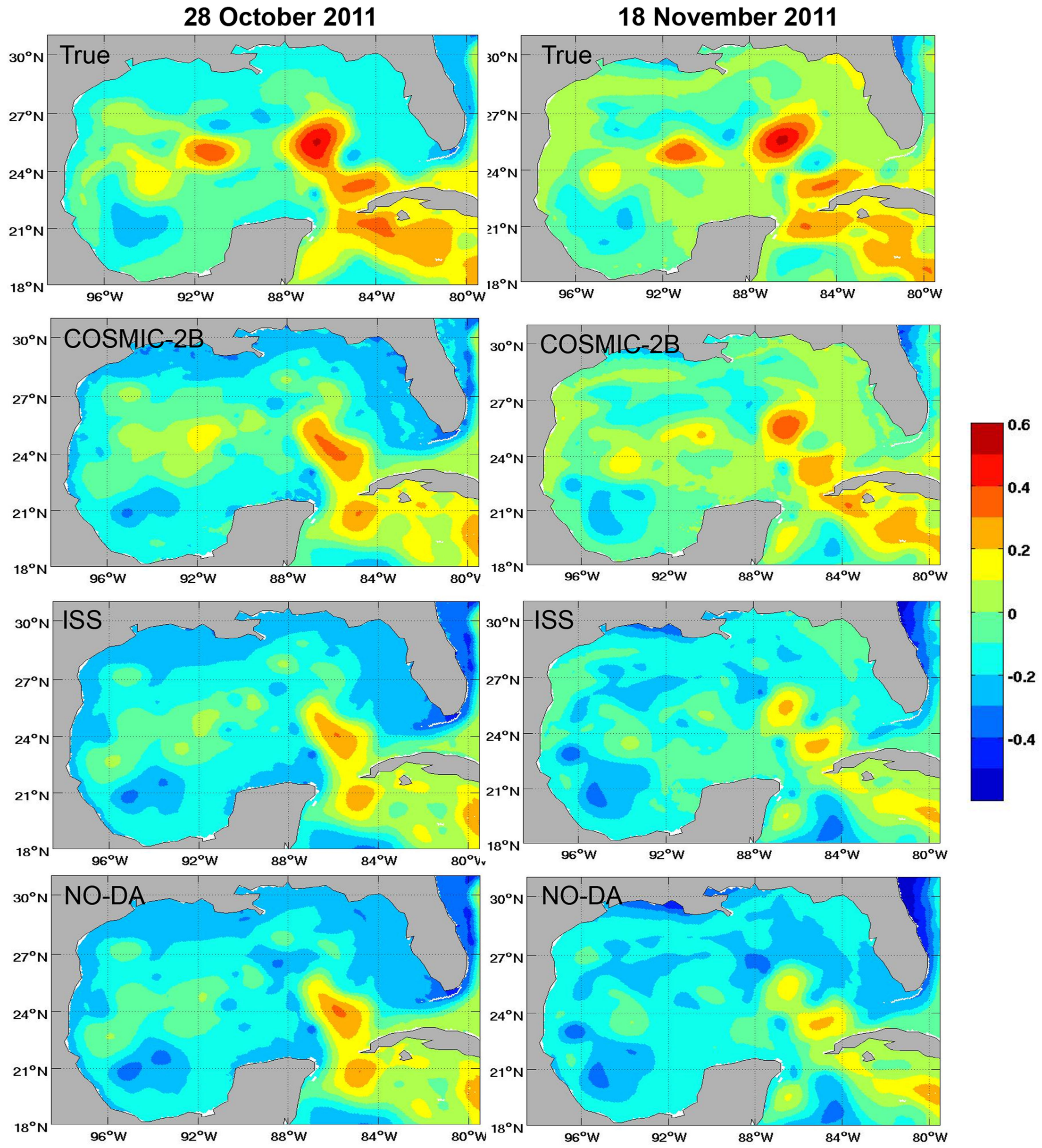

Fig. 24. Observing system simulation experiments (OSSEs) on the impact of GNSS-R SSHs on the eddy shedding in the Gulf of Mexico loop current. The maps are snapshots of SSHs (in m) on October 28 and November 18, 2011. The true state (True) is from a simulation of an eddy shedding event in November 2011. The regional ocean modeling system (ROMS) is used, and it has a horizontal resolution of 6 km. The ROMS model is initialized on October 15. The simulated observations are assimilated into the model every 12 h after the initialization. The observation errors have a Gaussian distribution with a mean of 0.5 m. The result from the OSSE for one receiver on board of ISS (ISS) is given, along with the result from six receivers following the COSMIC-2B constellation (COSMIC-2B) for a comparison. The experiment without data assimilation (NO-DA) is given as a control simulation.

assimilated by 4-D-VAR into a regional ocean model [73]. The performances of the different GNSS-R measurement configurations are evaluated by the assimilation's ability to recover the original oceanographic processes which lead to the observed SSH. The analysis is conduced scale-dependent to infer which processes can be resolved by assimilating GNSS-R observations. As shown in Fig. 25, all studied scales improve by the assimilation of SSH from GNSS-R. The most gain is found in the mesoscale between 500 and 3000 km with the maximum gain around 1000 km.

By comparing the RMS of different measurement configurations, it is demonstrated that the observation's precision is of minor importance. The high spatiotemporal density achievable by GNSS-R measurements is able to compensate the differences between code and phase precision. Consequently, limitations in the range of usable reflection angles and the connected reduction in observation density significantly impact the performance of the assimilation.

Due to the key role of the Agulhas region in Earth's climate [74], one of the study's main focus is the recovery of subsurface processes and transports, i.e., velocity, temperature, and salinity distributions down to the sea floor. Fig. 26 shows the temporal development of improvements that the assimilation of GNSS-R observations induces in the models velocity, temperature, and salinity. Although the GNSS-R-based SSH observations are only assimilated at 25% of the model domain's surface

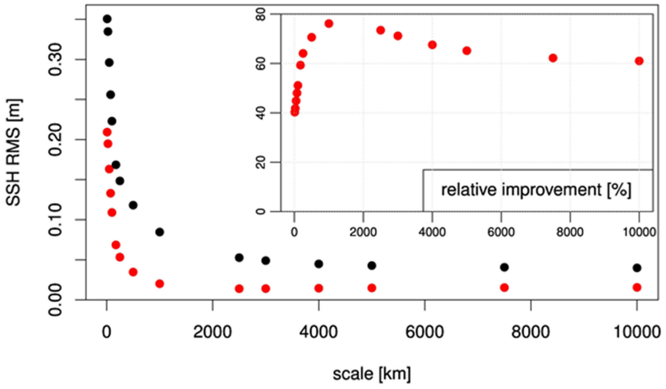

Fig. 25. Scale-dependence of sea surface height RMS-errors in the study region. Black dots: RMS-errors of the reference simulation. Red dots: RMS-errors of the GNSS-R assimilation. Inset: RMS-improvement (relative to the reference simulation) due to the assimilation of GNSS-R observations.

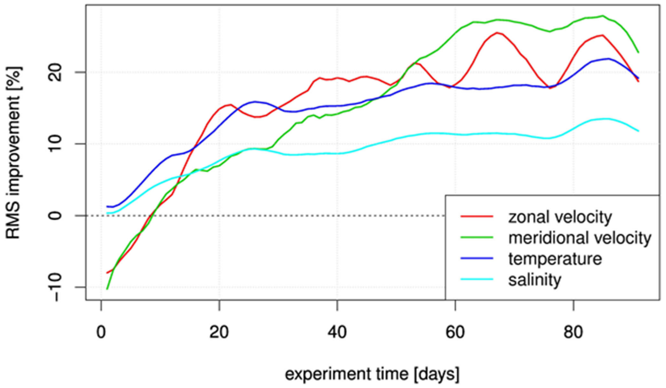

Fig. 26. Temporal development of RMS-improvements (3d-mean, relative to the reference simulation) of not assimilated oceanographic properties.

area, the RMS of all subsurface properties improves substantially throughout the domain.

In summary, the study provides a demonstration of the usefulness of GNSS-R observations to recover the true 3-D ocean state and the connected oceanographic processes. Furthermore, the study gives the recommendation that for oceanographic purposes GNSS-R missions should prioritize the optimization of FoV and reflection angle range over the optimization of precision.

3) NERSC: NERSC investigated the influence of simulated observation data from three different GEROS constellations against the present performance of state-of-the-art eddy-resolving ocean data assimilation system. It is expected that the reflectometer data can bring complementary data in the case of severe storms, so a regional HYCOM model of the South China Sea (SCS) was considered, equipped with an Ensemble optimal interpolation assimilation system for traditional along-track altimeter data and SST. The period of interest is July 2014 during which the SCS has been hit by the typhoon Ramasun. The model and assimilation systems are described in [75] and the simulated GEROS data, described in Section IV, are assimilated in addition to the "present day" observing system, together with their specified uncertainty properties. A "truth" run is generated by assimilation of (real) traditional altimeter and SST data, then its initial conditions are perturbed by a shift of the initial date tag and two runs are integrated without GEROS (standard observing system) and with GEROS data as would have been obtained from three observing scenarios: GEROS onboard the ISS, GEROS-FOV1 and FOV2 for two different FoVs (not shown here).

The results in Fig. 27 indicate that the GEROS data can improve the rendering of mesoscale features in the SCS over the satellite constellation that was active in July 2014. Statistics over the whole month of July 2014 indicate that the GEROS can reduce the RMS errors of sea level anomalies by 13%, which is a significant improvement in an operational ocean forecasting system, whereas the GEROS-FoV1 and FoV2 achieve even greater reductions by 20% and 29%, respectively.

C. *GNSS-R for Land Applications*

The low frequency band exploited by the navigation systems (i.e., typically L-band) is suitable for land applications, such as soil moisture and vegetation biomass monitoring, due to the reduced atmosphere attenuation, and especially the good penetration capability.

The ESA Living Planet Programme foresees, among others, a better understanding of the hydrological cycle throughout a mapping of the soil moisture at global scale, and the improvements of weather and flood forecasts by assimilating soil moisture observations into models. Vegetation constitutes the link between water cycle and carbon cycle, since moisture dynamics impacts vegetation structure and growth and, in turn, the soil–plant–atmosphere system. Forests, in particular, can store large amount of CO2, and therefore are involved in the carbon cycle, which influences greenhouse effect, global and local climatic change. Theoretical and experimental works have investigated the potential of GNSS-R for land applications. For instance, interference patterns between direct and reflected signals are exploited on ground to derive soil moisture and snow parameters. Although the sensitivity of the GNSS-R signal to the target land parameters has been proved, it has not been demonstrated the feasibility to exploit it from satellite in an operational way, yet. The application of GNSS-R over land was not included in the original GEROS proposal, but is regarded by the GEROS-SAG as an additional and important mission objective. In this respect, many functionalities foreseen for GEROS primary applications over ocean can be exploited for land as well. In particular, the highly flexible antenna operating in both circular polarizations shall provide independent pieces of information for land parameter retrieval, and its high gain will enable to sense a wide signal dynamic range, especially over dense vegetated targets (e.g., forests) with high attenuation.

ESA funded some exploratory studies to investigate these issues. In the frame of the "Land Monitoring with Navigation Signals" project a GNSS-R receiver, developed by Starlab Barcelona, was installed on a crane and registered the signal reflected from an agricultural area near Florence (Italy). An entire crop growing season was covered, with high variability of field moisture and roughness [76]. Electromagnetic models were implemented as a unique software package (i.e., SAVERS) able to predict the contribution of the coherent and incoherent scattering mechanisms to the waveforms and DDM's collected

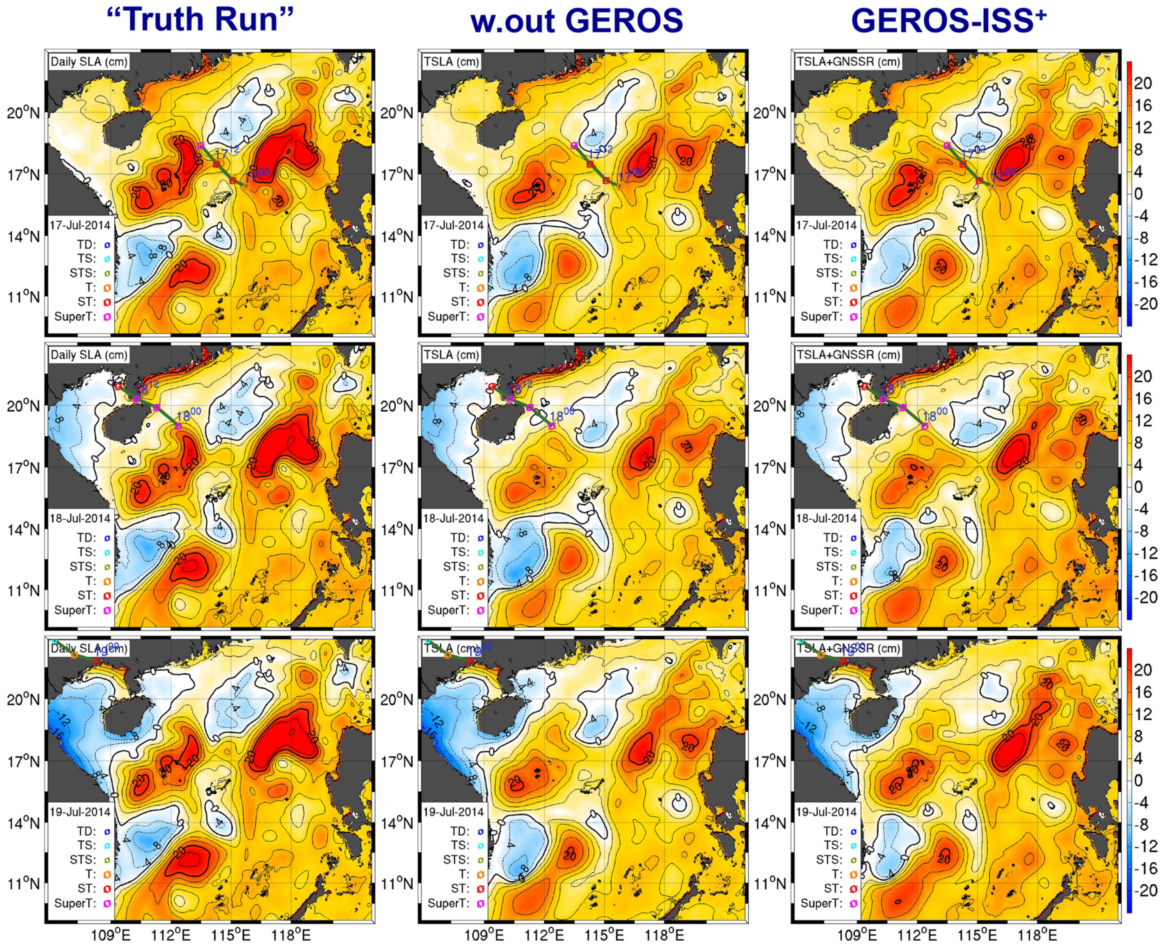

Fig. 27. Daily SLA maps of "Truth" (left), standard (middle), and GEROS-ISS runs (right) from 16 to 19 July, 2014 (unit: cm). The contour interval is 4 cm, and the green line indicates the Ramasun typhoon track during the 24 h of the daily average map. The symbols of "TD, TS, STS, T, ST, SUPER T" are related with the Tropical Cyclone Classification considering the maximum wind near the centre (km/h): TD: Tropical Depression (<63); TS: Tropical Storm (63–87); STS: Severe Tropical Storm (88–117); T: Typhoon (118–149); ST: Severe Typhoon (150–184); SuperT: Super Typhoon (≥ 185).

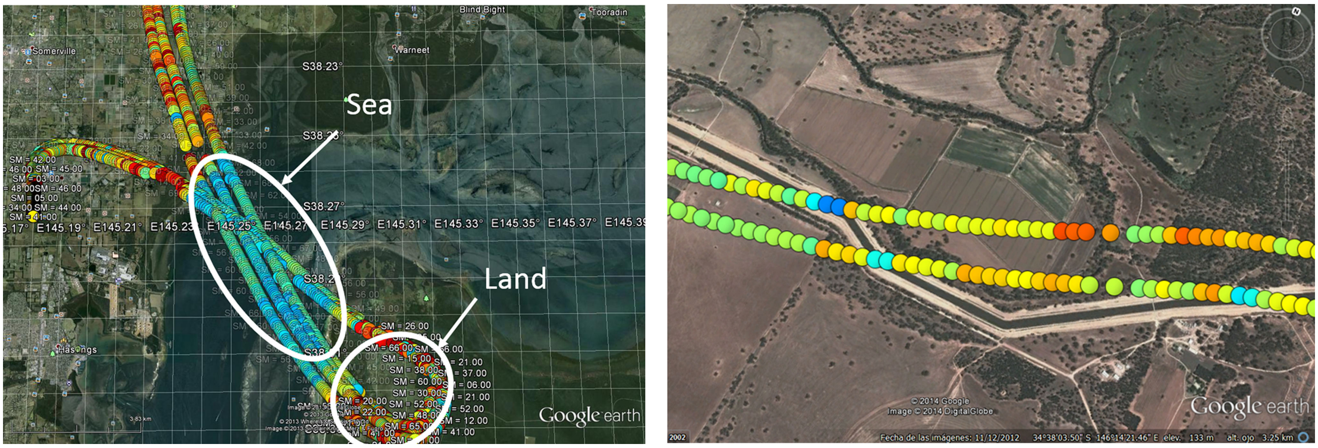

Fig. 28. Left: Sample ground-tracks of up to 4 simultaneous GNSS-R reflections after take-off Melbourne (Australia) collected with the LARGO instrument, and Right: sample ground-tracks showing the variability of the scattering coefficient over terrain and water bodies. The color scale represents the forward scattering coefficient (blue: high, red: low). The largest scattering is produced over water bodies, either the ocean (left image) or over water channels (right image). Over the ocean there is also variability due to different sea states (left). Over land (right plot), lower/higher scattering (red/blue) is associated with lower/higher soil moisture conditions (dry/moist soil). Surface roughness, vegetation, and topography effects also play a role in the magnitude of the scattering coefficient.

over bare and vegetated targets [77]. The simulator was further validated using data collected during the "GNSS Reflectometry Analysis for Biomass Monitoring" airborne experiment [78]. Major findings were the quantification of the sensitivity of the surface equivalent reflectivity to soil moisture and roughness, whose combined effects can been disjoined by exploiting polarimetric observations. Moreover, SAVERS correctly predicted the observed attenuation of the coherent signal reflected by the soil surface, which is directly linked to the above ground biomass of forests. Finally, new prospects can be opened up by combining the quasispecular observation of the GEROS reflectometer with backscatter data collected by radar systems overpassing the same area (e.g., Sentinel 1A or 1B). For instance, the increase of backscatter and decrease of specular reflectivity with soil roughness may help discriminating soil moisture from roughness variations using such a multistatic approach. GNSS-R applications over land have also been explored by other experiments:

1) two stratospheric balloon experiments (BEXUS-17/19) over boreal forests (Sweden and Finland) using the UPC PYCARO instrument (dual-frequency L1 + L2, dual polarization RHCP+LHCP, and multiconstellation: GPS, GLONASS, and Galileo),
2) two airborne experiments in Victoria (Australia) and Zamora (Spain) using the UPC LARGO (L1, C/A code, and LHCP only), and
3) using data from the U.K. TDS-1 (L1, C/A code, and LHCP only).

The BEXUS experiments showed a non-negligible coherent scattering component, with a power nearly constant with the platform height [12], a multimodal scattering behavior, showing different scattering mechanisms in the soil surface and vegetation [12], and a polarimetric ratio ranging from -2 down to -16 dB over different types of surfaces [79]. The airborne experiments demonstrated the sensitivity to soil moisture, water, but to vegetation and surface slopes as well [see Fig. 28(b), [80]]. Topography and variations of the local incidence angle have to be corrected, and it was found that a combined use of a water/vegetation index with GNSS-R reflectivity and land surface temperature significantly improves the soil moisture estimation [81]. Finally, the analysis of the TDS-1 dataset, collocated with SMOS level 3 soil moisture data, and MODIS NDVI data, found a significant sensitivity for nearly bare soils $\sim$38 dB/(m^3/m^3), with a high Pearson correlation parameter $R = 0.63$, although vegetation effects [37] were clearly noticeable, as well as topography effects, whose correction will require further analysis due to the larger footprint than in airborne experiments.

We briefly mention here also the high potential of GNSS-R for snow surface monitoring (see, e.g., [82], [83]), which is not a main driver of the mission. This application was not investigated in detail during the recent GEROS preparation phase, but is expected to be focussed more during the course of the mission.

VI. SUMMARY AND OUTLOOK

This paper gave a description and status overview of ESA's ISS experiment, GEROS, which seeks to exploit signals of opportunity from GNSS for ocean, atmosphere, and land cover remote sensing. GEROS represents the first dedicated experiment to assess the usefulness of spaceborne GNSS-R to detect and map ocean surface height at the mesoscale (10–100 km or longer scale) under all-weather conditions. The GEROS measurements of SSH will complement SSH data from the multisatellite constellation of traditional radar altimeters, leading to better monitoring of the ocean mesoscale variability at a finer spatial scale closer to 10 km, which is not achievable by current nadir altimeters. A major advance afforded by the GEROS dataset will be to determine the value of GNSS-R as a means of providing long-term sustained observations of eddies and their variability. Moreover, GEROS will not only demonstrate GNSS-R for sea surface altimetry and confirm its performance, it will also allow to consolidate the required technology, provide data to mature science and develop data-processing techniques. To this end, GEROS will make use of the unique ISS platform to generate an unprecedented dataset to advance the exploitation of GNSS-based Earth observation techniques to provide climate-relevant measurements, which represent the forerunner of potential future operational missions capable of delivering a long-term climate record of the Earth. After successful completion of Phase A, the feasibility phase, GEROS is now ready to enter the implementation phases with an eventual launch in 2020.

REFERENCES

[1] J. Wickert *et al.*, "GNSS rEflectometry, radio occultation and scatterometry onboard ISS for long-term monitoring of climate observations using innovative space geodetic techniques on-board the international space station," *Proposal in response to call: European Space Agency Research Announcement for International Space Station Experiments relevant to study of Global Climate Change*, 2011, p. 80.

[2] K. Flechter, M. Rast, and M. Kern, Eds., *Earth Observation Science Strategy for ESA: A New Era for Scientific Advances and Societal Benefits*. Paris, France: ESA, 2015. [Online]. Available: http://esamultimedia.esa.int/multimedia/publications/SP-1329_1

[3] K. Flechter, M. Rast, and M. Kern, Eds., *ESA's Living Planet Programme: Scientific Achievements and Future Challenges*. Paris, France: ESA, 2015. [Online]. Available: http://esamultimedia.esa.int/multimedia/publications/SP-1329_2

[4] R. Stosius, G. Beyerle, A. Helm, A. Hoechner, and J. Wickert, "Simulation of space-borne tsunami detection using GNSS-Reflectometry applied to tsunamis in the indian ocean," *Natural Hazards Earth Syst. Sci.*, vol. 10, no. 6, pp. 1359–1372, 2010.

[5] R. Stosius, G. Beyerle, A. Hoechner, J. Wickert, and J. Lauterjung, "The impact on tsunami detection from space using GNSS-reflectometry when combining GPS with GLONASS and Galileo," *Adv. Space Res.*, vol. 47, no. 5, pp. 843–853, 2011.

[6] C. Ruf *et al.*, "The CYGNSS nanosatellite constellation hurricane mission," in *Proc. 2012 Int. Geosci. Remote Sens. Symp.*, Munich, Germany, Jul. 20–27, 2012, pp. 214–216.

[7] A. J. Mannucci, C. Ao, L. Young, and T. Meehan, "Studying the atmosphere using global navigation satellites," *EOS Trans.*, vol. 95, no. 43, pp. 389–390, 2014.

[8] C. Zuffada *et al.*, "A constellation for high resolution sea surface topography with frequent temporal revisit," White Paper, Jet Propulsion Laboratory, California Inst. Technol. Pasadena, CA, USA, 2005.

[9] GEROS-SAG and GEROS-ESA-Team, "GEROS mission requirements document," ESA, Paris, France, Tech. Rep. EOP-SM/2587/MK-mk, 2013.

[10] GEROS-ESA-Team, "GEROS system requirements document," ESA, Paris, France, Tech. Rep. TEC-ETP/2013.202/MMN, 2013.

[11] G. Foti *et al.*, "Spaceborne GNSS reflectometry for ocean winds: First results from the UK TechDemoSat-1 mission," *Geophys. Res. Lett.*, vol. 42, no. 13, pp. 5435–5441, 2015. [Online]. Available: http://dx.doi.org/10.1002/2015GL064204

[12] H. Carreno-Luengo, A. Camps, P. Via, J. F. Munoz, A. Cortiella, D. Vidal, J. Jane, N. Catarino, M. Hagenfeldt, P. Palomo, and S. Cornara, "3CAT-2: An experimental nanosatellite for GNSS-R Earth opbservation: Mission concept and analysis," *IEEE J. Sel. Topics Appl. Earth Observ. Remote Sens.*, vol. 9, no. 10, pp. 4540–4551, doi: 10.1109/JSTARS.2016.2574717.

[13] N. Catarino *et al.*, "METH-10-E-GEM: European GNSS-R environmental monitoring," Project FP7-SPACE-2013-1, Tech. Rep. METH-10-E-GEM, DEIMOS, Lisbon, 2013.

[14] J. Wickert *et al.*, "GARCA: Proposal in response to AO/1-7850/14/NL/MV: GNSS-R assessment of requirements and consolidation of retrieval algorithms," ESA/ESTEC, Noordwijk, The Netherlands, Tech. Rep., AO/1-7850/14/NL/MV, May 2014.

[15] F. Soulat *et al.*, "GARCA Technical Note 1: Review of the state-of-the-art and consolidation of the requirements," ESA/ESTEC, Noordwijk, The Netherlands, Tech. Rep. ESA-AO1-7850/14-GARCA-TN-1, Mar. 2015.

[16] H. Park *et al.*, "GARCA Technical Note 2: Algorithm theoretical baseline document for the GEROS-SIM internal algorithms," ESA/ESTEC, Noordwijk, The Netherlands, Tech. Rep. ESA-AO1-7850/14-GARCA-TN-2, Aug. 2015.

[17] C. Gommenginger *et al.*, "GARCA Technical Note 3: Validation and test plan," ESA/ESTEC, Noordwijk, The Netherlands, Tech. Rep. ESA-AO1-7850/14-GARCA-TN-3, Dec. 2015.

[18] E. Cardellach *et al.*, "GARCA Technical Note 4: Data Acquisition and Analysis Report," ESA/ESTEC, Noordwijk, The Netherlands, Tech. Rep. ESA-AO1-7850/14-GARCA-TN-4, 2016.

[19] L. Bertino *et al.*, "GARCA Technical Note 5: Impacts of SLA observations derived from GEROS-ISS into the current oceanographic system," ESA/ESTEC, Noordwijk, The Netherlands, Tech. Rep., ESA-AO1-7850/14-GARCA-TN-5, 2016.

[20] E. Cardellach and A. Rius, "GARCA Technical Note 6: OSSE synthetic observations," ESA/ESTEC, Noordwijk, The Netherlands, Tech. Rep. ESA-AO1-7850/14-GARCA-TN-6, Sep. 2015.

[21] M. Semmling *et al.*, "Sea surface topography retrieved from GNSS reflectometry phase data of the GEOHALO flight mission," *Geophys. Res. Lett.*, vol. 41, pp. 954–960, 2014.

[22] M. Martín-Neira, S. D'Addio, C. Buck, N. Floury, and R. Prieto-Cerdeira, "The PARIS ocean altimeter In-Orbit demonstrator," *IEEE Trans. Geosci. Remote Sens.*, vol. 49, no. 6, pp. 2209–2237, Jun. 2011.

[23] A. Camps *et al.*, "Optimization and performance analysis of interferometric GNSS-R altimeters: Application to the PARIS IoD mission," *IEEE J. Sel. Topics Appl. Earth Observ. Remote Sens.*, vol. 7, no. 5, pp. 1436–1451, May 2014.

[24] H. Park, A. Camps, D. Pascual, A. Alonso, F. Martin, and H. Carreno-Luengo, "Improvement of the PAU/PARIS end-to-end performance simulator (P2EPS) in preparation for upcoming GNSS-R missions," in *Proc. IEEE Int. Geosci. Remote Sens. Symp.*., Jul. 2013, pp. 362–365.

[25] F. Martín, "Interferometric GNSS-R processing: Modeling and analysis of advanced processing concepts for altimetry," Ph.D. dissertation, Universitat Politècnica de Catalunya, Barcelona, Spain, 2000. [Online]. Available: http://www.tdx.cat/handle/10803/316583

[26] Earth Observation CFI Software, v. 10, Oct. 29, 2015. [Online]. Available: http://eop-cfi.esa.int/index.php/mission-cfi-software/eocfi-software

[27] J. Bandeiras, A. Sousa, S. Tonetti, N. Catarino, F. Benito, and M. Martín-Neira, "GEROS-ISS: Analysis of reflection points," *IEEE Int. Geosci. Remote Sens. Symp.*, Milan, Italy, 2015, pp. 4781–4784.

[28] V. Zavorotny and A. Voronovich, "Scattering of GPS signals from the ocean with wind remote sensing application," *IEEE Trans. Geosci. Remote Sens.*, vol. 38, no. 2, pp. 951–964, Mar. 2000.

[29] H. Park *et al.*, "End-to-end simulator for global navigation satellite system reflectometry space mission," in *Proc. IEEE Int. Geosci. Remote Sens. Symp.*, Jul. 2010, pp. 4294–4297.

[30] J. F. Marchan-Hernandez, A. Camps, N. Rodriguez-Alvarez, E. Valencia, X. Bosch-Lluis, and I. Ramos-Perez, "An efficient algorithm to the simulation of delay doppler maps of reflected global navigation satellite system signals," *IEEE Trans. Geosci. Remote Sens.*, vol. 47, no. 8, pp. 2733–2740, Aug. 2009.

[31] H. Park, D. Pascual, F. Martin, E. Valencia, and A. Camps, "Contribution to system end-to-end performance model and validation report," Tech. Univ. Catalonia, Barcelona, Spain, Tech. Rep. PARISPhA-IEEC-UPC-TN-11, 2012.

[32] S. T. Lowe, C. Zuffada, Y. Chao, P. Kroger, L. E. Young, and J. L. LaBrecque, "5-cm precision aircraft ocean altimetry using GPS reflections," *Geophys. Res. Lett.*, vol. 29, no. 10, p. 13-1–13-4, 2002.

[33] G. A. Hajj and C. Zuffada, "Theoretical description of a bistatic system for ocean altimetry using the GPS signal," *Radio Sci.*, vol. 38, no. 5, pp. 1–10, 2003.

[34] A. Rius, E. Cardellach, and M. Martín-Neira, "Altimetric analysis of the sea-surface GPS-reflected signals," *IEEE Trans. Geosci. Remote Sens.*, vol. 48, no. 4, pp. 2119–2127, Apr. 2010.

[35] E. Cardellach *et al.*, "Consolidating the precision of interferometric GNSS-R ocean altimetry using airborne experimental data," *IEEE Trans. Geosci. Remote Sens.*, vol. 52, no. 8, pp. 4992–5004, Aug. 2014.

[36] M. P. Clarizia, C. Ruf, P. Cipollini, and C. Zuffada, "First spaceborne observation of sea surface height using GPS-Reflectometry," *Geophys. Res. Lett.*, vol. 43, pp. 767–774, 2016.

[37] A. Camps, H. Park, M. Pablos, G. Foti, C. P. Gommenginger, P. W. Liu, and J. Judge, "Sensitivity of GNSS-R spaceborne observations to soil moisture and vegetation," *IEEE J. Sel. Topics Appl. Earth Observ. Remote Sens.*, vol. PP, no. 99, pp. 1–13, doi: 10.1109/JSTARS.2016.2588467.

[38] B. Hofmann-Wellenhof, H. Lichtenegger, and E. Wasle, *GNSS Global Navigation Satellite Systems—GPS, GLONASS, Galileo & more*. New York, NY, USA: Springer, 2008.

[39] A. Camps, H. Park, A. Ghavidel, J. M. Rius, and I. Sekulic, "GEROS-ISS, a demonstration mission of GNSS remote sensing capabilities to derive geophysical parameters of the earth surfaces: Altimetry performance evaluation," in *Proc. IEEE Int. Geosci. Remote Sens. Symp.*, Jul. 2015, pp. 3917–3920.

[40] S. D'Addio, M. Martín-Neira, M. di Bisceglie, C. Galdi, and F. Martín Alemany, "GNSS-R Altimeter based on doppler multi-looking," *IEEE J. Sel. Topics Appl. Earth Observ. Remote Sens.*, vol. 7, no. 5, pp. 1452–1460, May 2014.

[41] W. Bosch, R. Savcenko, D. Dettmering, and C. Schwatke, "A two-decade time series of eddy-resolving dynamic ocean topography (iDOT)," in *Proc. 20 Years of Progress in Radar Altimetry Symp.*, Sept. 2012, Venice, Italy, ESA SP-710 (CD-ROM), ISBN 978-92-9221-274-2, ESA/ESTEC, 2013.

[42] E. Cardellach, C. Ao, M. de la Torre Juarez, and G. Hajj, "Carrier phase delay altimetry with GPS–reflection/occultation interferometry from low Earth orbiters," *Geophys. Res. Lett.*, vol. 31, 2004, Art. no. L10 402, doi:10.1029/2004GL019 775.

[43] A. M. Semmling, G. Beyerle, J. Beckheinrich, M. Ge, and J. Wickert, "Airborne GNSS reflectometry using crossover reference points for carrier phase altimetry," in *Proc. IEEE Int. Geosci. Remote Sens. Symp*. Quebec City, QC, Canada, 2014, pp. 3786–3789.

[44] A. M. Semmling, V. Leister, J. Saynisch, F. Zus, S. Heise, and J. Wickert, "A phase-altimetric simulator: Studying the sensitivity of Earth-reflected GNSS signals to ocean topography," *IEEE Trans. Geosci. Remote Sens.*, vol. 54, no. 11, pp. 6791–6802, Nov. 2016.

[45] C. Förste *et al.*, "EIGEN-6C4 The latest combined global gravity field model including GOCE data up to degree and order 2190 of GFZ Potsdam and GRGS Toulouse," *GFZ Data Services*, 2014. [Online]. Available: http://doi.org/10.5880/icgem.2015.1

[46] R. Shako *et al.*, "High-resolution global gravity fields by combining GOCE, GRACE and terrestrial data: First result from the REAL GOCE project," *GEOTECHNOLOGIEN Sci. Rep.*, vol. 17, pp. 112–117, 2010. [Online]. Available: http://doi.org/10.2312/GFZ.gt.17.17

[47] O. Andersen and P. Knudsen, "The DNSC08 mean sea surface and mean dynamic topography," *J. Geophys. Res.*, vol. 114, no. C11, 2009, Art. no. C11001.

[48] A. Alonso-Arroyo, A. Camps, H. Park, D. Pascual, R. Onrubia, and F. Martín, "Retrieval of significant wave height and mean sea surface level using the GNSS-R interference pattern technique: Results from a three-month field campaign," *IEEE Trans. Geosc. Remote Sens.*, vol. 53, no. 6, pp. 3198–3209, Jun. 2015.

[49] S. Gleason *et al.*, "Detection and processing of bistatically reflected GPS signals from low Earth orbit for the purpose of ocean remote sensing," *IEEE Trans. Geosci. Remote Sens.*, vol. 43, no. 6, pp. 1229–1241, Jun. 2005.

[50] S. Gleason, "Remote sensing of ocean, ice and land surfaces using bistatically scattered GNSS signals from low Earth orbit," Ph.D. dissertation, University of Surrey, Guildford, U.K., 2006.

[51] S. Gleason and D. Gebre-Egziabher, *GNSS Applications and Methods*. Norwood, MA, USA: Artech House, 2009.

[52] M. Clarizia, C. Gommenginger, S. Gleason, M. Srokosz, C. Galdi, and M. Di Bisceglie, "Analysis of GNSS-R delay-Doppler maps from the UK-DMC satellite over the ocean," *Geophys. Res. Lett.*, vol. 36, no. 2, 2009, Art. no. L02608.

[53] H. Bock, A. Jäggi, G. Beutler, and U. Meyer, "GOCE: Precise orbit determination for the entire mission," *J. Geodesy*, vol. 88, no. 11, pp. 1047–1060, 2014.

[54] C. Flohrer, M. Otten, T. Springer, and J. Dow, "Generating precise and homogeneous orbits for Jason-1 and Jason-2," *Adv. Space Res.*, vol. 38, p. 152–172, 2011.

[55] C. Reigber, H. Lühr, P. Schwintzer, and Wickert, Eds., *Earth Observation With CHAMP: Results From Three Years in Orbit*. Berlin, Germany: Springer, 2005.

[56] S. Heise, J. Jakowski, A. Wehrenpfennig, C. Reigber, and H. Lühr, "Sounding of the topside ionosphere/plasmasphere based on GPS measurements from champ: Initial result," *Geophys. Res.*, vol. 29, no. 14, pp. 44-1–44-4, 2002.

[57] H. Bock *et al.*, "GPS-derived orbits for the GOCE satellite," *J. Geodesy*, vol. 85, no. 11, pp. 807–818, 2011.

[58] O. Montenbruck, S. Rozkov, A. Semenov, S. Gomez, R. Nasca, and L. Cacciapuoti, "Orbit determination and prediction of the international space station," *J. Spacecraft Rockets*, vol. 48, no. 6, pp. 1055–1067, 2011.

[59] R. A. Anthes *et al.*, "THE COSMIC/FORMOSAT-3 MISSION: Early results," *Bull. Amer. Meteorol. Soc.*, vol. 89, no. 3, pp. 313–333, 2008. [Online]. Available: http://dx.doi.org/10.1175/BAMS-89-3-313

[60] J. Wickert *et al.*, "GPS radio occulation: Results from CHAMP, GRACE and FORMOSAT-3/COSMIC," *Terr. Atmos. Ocean. Sci.*, vol. 1, pp. 35–50, 2009.

[61] E. Cardellach *et al.*, "Sensitivity of PAZ LEO polarimetric GNSS radio-occultation experiment to precipitation events," *IEEE Trans. Geosci. Remote Sens.*, vol. 53, no. 1, pp. 190–206, Jan. 2015.

[62] R. Padullés *et al.*, "Atmospheric polarimetric effects on GNSS radio occultations: The ROHP-PAZ field campaign," *Atmos. Chem. Phys.*, vol. 16, pp. 635–649, Jan. 2016.

[63] G. Beyerle, K. Hocke, J. Wickert, T. Schmidt, C. Marquardt, and C. Reigber, "GPS radio occultations with CHAMP: A radio holographic analysis of GPS signal propagation in the troposphere and surface reflections," *J. Geophys. Res.*, vol. 107, pp. ACL 27-1–ACL 27-14, 2002, doi:10.1029/2001JD001 402.

[64] M. Martín-Neira, "GNSS interferometric radio occultation," *IEEE Trans. Geosci. Remote Sens.*, vol. 54, no. 6, pp. 5285–5300, Sep. 2016.

[65] A. Rius *et al.*, "Altimetry with GNSS-R interferometry: First proof of concept experiment," *GPS Solutions*, vol. 16, no. 2, pp. 231–241, 2011. [Online]. Available: http://dx.doi.org/10.1007/s10291-011-0225-9

[66] R. Atlas, "Atmospheric observations and experiments to assess their usefulness in data assimilation," *J. Meteorol. Soc. Japan*, vol. 75, pp. 111–130, 1997.

[67] S. Lord, J. Kalnay, R. Daley, G. Emmitt, and R. Altas, "Using OSSEs in the design of future generation integrated observing systems," in *Proc. 1st Symp. Integr. Observing Syst.,* Long Beach, CA, USA, 1997, pp. 45–47.

[68] Z. Li, Y. Chao, J. Farrara, and J. McWilliams, "Impacts of distinct observations during the 2009 Prince William Sound Field Experiment: A data assimilation study," *Continental Shelf Res.*, vol. 63, pp. 209–222, 2012.

[69] Z. Li, J. McWilliams, K. Ide, and J. Fararra, "Coastal ocean data assimilation using a multi-scale three-dimensional variational scheme," *Ocean Dyn.*, vol. 65, no. 7, pp. 1001–1015, 2015.

[70] Z. Li, J. McWilliams, K. Ide, and J. Fararra, "A multi-scale data assimilation scheme: Formulation and illustration," *Monthly Weather Rev.*, vol. 143, pp. 3804–3822, 2015.

[71] Z. Li, C. Zuffada, S. Lowe, T. Lee, and V. Zlotnicki, "Analysis on GNSS-R altimetry for mapping ocean mesoscale sea surface heights using high-resolution model simulations," *IEEE J. Sel. Topics Appl. Earth Observ. Remote Sens.*, 2016, doi: 10.1109/JSTARS.2016.2581699.

[72] J. Saynisch, M. Semmling, J. Wickert, and M. Thomas, "Potential of space-borne GNSS reflectometry to constrain simulations of the ocean circulation," *Ocean Dyn.*, vol. 65, no. 11, pp. 1441–1460, 2015.

[73] A. Moore *et al.*, "The regional ocean modeling system (roms) 4-dimensional vavariation data assimilation systems part iii - observation impact and observation sensitivity in the California current system," *Prog. Oceanogr.*, vol. 91, no. 1, pp. 74–94, 2011.

[74] W. Weijer and E. van Sebille, "Impact of agulhas leakage on the atlantic overturning circulation in the CCSM4," *J. Climate*, vol. 27, no. 1, pp. 101–110, 2014.

[75] J. Xie, J. Zhu, L. Bertino, and F. Counillon, "Analysis of the northern South China Sea counter-wind current in winter using a data assimilation model," *Ocean Dyn.*, vol. 65, no. 4, pp. 523–538, 2015.

[76] A. Egido *et al.*, "Global navigation satellite systems reflectometry as a remote sensing tool for agriculture," *Remote Sens.*, vol. 4, pp. 2356–2372, 2012.

[77] N. Pierdicca, L. Guerriero, R. Giusto, M. Brogioni, and A. Egido, "SAVERS: An end-to-end simulator of GNSS reflections from bare and vegetated soils," *IEEE Trans. Geosci. Remote Sens.*, vol. 52, no. 10, pp. 6542–6554, Oct. 2014.

[78] A. Egido *et al.*, "Airborne GNSS-R polarimetric measurements for soil moisture and Above-Ground biomass estimation," *Sel. Topics Appl. Earth Observ. Remote Sens.*, vol. 7, no. 5, pp. 1522–1532, 2014.

[79] H. Carreno-Luengo, A. Amezaga, D. Vidal, R. Olivé, J. Munoz, and A. Camps, "First polarimetric GNSS-R measurements from a stratospheric flight over boreal forests," *Remote Sens.*, vol. 7, pp. 13120–13138, 2015.

[80] A. Alonso-Arroyo *et al.*, "The light airborne reflectometer for GNSS-R observations (LARGO) instrument: Initial results from airborne and Rover field campaigns," *Geosci. Remote Sens. Symp.*, Quebec City, QC, Canada, 2014, pp. 4054–4057.

[81] N. Sánchez *et al.*, "On the synergy of airborne GNSS-R and Landsat 8 for soil moisture estimation," *Remote Sens.*, vol. 7, pp. 9954–9974, 2015.

[82] E. Cardellach, F. Fabra, A. Rius, S. Pettinato, and S. D'Addio, "Characterization of dry-snow sub-structure using gnss reflected signals," *Remote Sensing Environ.*, vol. 124, pp. 122–134, 2012.

[83] N. Rodriguez-Alvarez, A. Aguasca, E. Valencia, X. Bosch-Lluis, A. Camps, I. Ramos-Perez, H. Park, M. Vall-llossera, "Snow Thickness Monitoring Using GNSS Measurements," in *IEEE Geosci. Remote Sens. Lett.*, vol. 9, no. 6, pp. 1109–1113, Nov. 2012. doi: 10.1109/LGRS.2012.2190379

Jens Wickert received the graduate degree in physics from the Technical University Dresden, Dresden, Germany, and the Ph.D. degree in geophysics/meteorology from the Karl-Franzens-University Graz, Austria, in 1989 and 2002, respectively.

He worked for several German geoscience research institutes and currently holds a joint Professorship of GFZ and Technical University Berlin on Global Navigation Satellite Systems (GNSS) Remote Sensing, Navigation and Positioning. In addition he is the Deputy GFZ Section Head Space Geodetic Techniques and the GFZ Speaker of the Atmosphere and Climate research programme of the German Helmholtz Association. Wickert was Principal Investigator of the pioneering GPS Radio Occultation experiment aboard the German CHAMP satellite and was coordinating the GEROS-ISS proposal to ESA. He is the Chair of the Science Advisory Group of the GEROS-ISS mission and author/coauthor of more than 160 ISI listed publications on GNSS Earth Observation.

Estel Cardellach (M'10) received the Ph.D. degree in physics from the Polytechnic University of Catalonia, Barcelona, Spain, in 2002.

She has been working on scientific applications of global navigation satellite systems (GNSS) for remote sensing of the Earth, such as extraction of geophysical information of the GNSS reflected signals, radio occultation, and geodetic techniques. She was a National Research Council Awardee for a postdoctoral position at NASA/Jet Propulsion Laboratory, Pasadena, CA (2002–2003); a Postdoctoral Researcher at Harvard Smithsonian Center for Astrophysics, Cambridge, MA, USA (2003–2005). Since 2005, she has been with the Institute of Space Sciences (ICE-CSIC/IEEC), currently under the Spanish Ramón y Cajal program. She is the Principal Investigator of the space-borne experiment *Radio-Occultation and Heavy Precipitation* aboard the PAZ Low Earth Orbiter.

Dr. Cardellach is a member of the GEROS-ISS proposing team and the Co-Chair of the GEROS Scientific Advisory Group.

Manuel Martín-Neira (SM'96) received the M.S. and Ph.D. degrees in telecommunication engineering from the School of Telecommunication Engineering, Polytechnic University of Catalonia, Barcelona, Spain, in 1986 and 1996, respectively.

In 1988, he was awarded a fellowship to work on microwave radiometry at ESA (European Space Agency), in The Netherlands. From 1989 to 1992, he joined GMV, a Spanish firm, as responsible for several projects on GPS spacecraft precise navigation and attitude determination, and since 1992, with ESA, in charge of the radiometer activities within the Payload, Equipment and Technology Section. He has developed new concepts for constellations of small satellites for Earth Observation. In particular, he holds several patents related to aperture synthesis radiometry and on the use of global navigation satellite systems signals reflected from the ocean (PARIS concept). Since 2001, he is the Instrument Principal Engineer of ESA's Soil Moisture and Ocean Salinity mission. Since 2008, he has been also working in potential GNSS reflectometry missions like the PARIS In-orbit Demonstration mission and the GEROS-ISS experiment on the International Space Station.

Dr. Martín-Neira received the Confirmed Inventor Award from ESA in 2002, the Salva i Campillo Award and the Premio Jaime I in 2010 from Spain, and a Certificate of Recognition for the SMOS mission in 2011 from IEEE. He is a member of the Academie des Technologies of France.

Jorge Bandeiras received the first degree in applied mathematics and computer science from Instituto Superior Técnico, Lisbon, Portugal, in 2006.

He is a Senior Project Engineer, with a large experience in the development of algorithms and software for the space sector, namely for ESAs projects. He was a Technical Leader and a Project Engineer for several projects related mainly to data processing and end-to-end instrument simulation, including the development of the SARGO GNSS Reflectometry system (within the FP7 E-GEM project), the development of the simulators for generic microwave radiometers (SAIRPS), and has participated in the development of the Sentinel 3 Surface Topographic Simulator (SRAL-SG and MWR-GPP), in the Galileo Independent Orbits and Clocks Estimation of GALSEE validation facility and in GNSS navigation studies (AGGA4VAL and CloseSearch).

Laurent Bertino received the Doctorate degree in geostatistics from the Ecole des Mines de Paris, Paris, France, in 2001.

He has 13 years of experience in pluri-disciplinary applications of data assimilation with the ensemble Kalman filter, in particular with coupled ice-ocean data assimilation and operational forecasting in the Arctic. He is currently a Research Director at Nansen Environmental and Remote Sensing Center, Leader of the Data Assimilation group and of the Arctic MFC in the Copernicus Marine Environment Monitoring Services.

Ole Baltazar Andersen received the graduate degree in geophysics from the University of Aarhus, Aarhus, Denmark, and the Ph.D. degree in geophysics from the University of Copenhagen, Copenhagen, Denmark, in 1996.

He has worked for the National Survey and the Danish National Space Center and is currently a Senior Research Scientist at DTU Space, Technical University of Denmark, Kgs. Lyngby, Denmark. He heads the section on marine remote sensing in the geodetic division focusing on subjects like altimetric gravity, ocean tides, and dynamics and sea level and climate change on global and regional scales. He has authored/co-authored more than 130 peer-reviewed publications.

Adriano Camps (FM'90) was born in Barcelona, Spain, in 1969. He received the degree in telecommunications engineering and the Ph.D. degree from the Universitat Politcnica de Catalunya (UPC), Barcelona, Spain, in 1992 and 1996, respectively.

In 1991–1992, he was with the ENS des Telecommunications de Bretagne, France. Since 1993, he has been with the Electromagnetics and Photonics Engineering Group, Department of Signal Theory and Communications, UPC. In 1999, he was on sabbatical leave at the Microwave Remote Sensing Laboratory, University of Massachusetts, Amherst, MA, USA. Since 1993, he has been involved in the European Space Agency SMOS Earth Explorer Mission, since 2000 in the use of global navigation satellite systems reflectometry techniques to perform the sea state correction needed to retrieve salinity from radiometric observations, as well as for soil moisture, vegetation, and altimetry applications, and since 2007 in the development of small satellites to test new techniques and sensors for earth observation.

Nuno Catarino received the first degree in physics engineering from the Instituto Superior Técnico, Lisbon, Portugal, and the Ph.D. degree in applied mathematics from the University of Warwick, Coventry, U.K., in 2000 and 2004, respectively.

He is the Head of PDGS Division in the Ground Segment Systems Business Unit, DEIMOS Engenharia, Lisboa, Portugal. He is currently the Coordinator of the H2020 Co-ReSyF and E-GEM projects, and is responsible for the SARGO product development, using GNSS-R technologies. He has led many projects for ESA and other clients, namely the GNSS-R projects PARIS IOD and GEROS-ISS Phase A studies, the GARCA scientific studies, the GEAF intelligent Ground Segment orchestrator, and the Sentinel 3 Optical Ground Processor Level 1 Prototype at DEIMOS Engenharia, Lisboa, Portugal. He has also participated in the Phases 3 and 4 of the SMOS L1 Processor Prototype, including the Image Validation Campaign at ESRIN and the re-design and implementation of the Image Reconstruction Module.

Bertrand Chapron received the Ph.D. degree in fluid mechanics from Aix-Marseille II, Marseille, France, in 1988.

He is the Head of the Space Oceanography Laboratory at Institut Franais de Recherche Pour l'exploitation de la Mer, Paris, France, responsible for the Centre Exploitation and Research for Satellite data. He has broad background in the use of satellite data for ocean remote sensing and oceanography in general and participates in numerous related national and international satellite and research projects. He published more than 100 papers in refereed journals in applied mathematics, physical oceanography, electromagnetic wave theory, and its applications to ocean remote sensing, data processing and management.

Fran Fabra received the M.Sc. degree in telecommunication engineering, in 2007, the Master's degree in information and communication technologies from Universitat Politècnica de Catalunya, in 2007, and the Ph.D. degree from the Universitat Politecnica de Catalunya, Barcelona, Spain, in 2013. He developed his Master's thesis on security in aeronautical mobile networks at TriaGnoSys GmbH, Munich, Germany. His Ph.D. dissertation was dedicated to research of the GNSS-R concept toward remote sensing of the cryosphere.

He is with the Earth Observation Research Group, Institute of Space Sciences (ICE-CSIC/IEEC), Barcelona, Spain, where he works on applications of global navigation satellite systems to Earth science.

Nicolas Floury received the Diplome d'Ingénieur degree from the Ecole Nationale Superieure des Télećommunications, Paris, France, in 1993, and the Ph.D. degree from the Université Paris 7 Denis Diderot, Paris, in 1999.

Since 1999, he has been with the European Space Research and Technology Centre, European Space Agency, Noordwijk, The Netherlands, where he is heading the Wave Interaction and Propagation Section. His research interests include signal processing and electromagnetic modeling applied to microwave interaction with natural media.

Giuseppe Foti received the M.Eng. degree in electronics engineering from the University of Catania, Catania, Italy, in 2000, and the M.Sc. degree in oceanography from the University of Southampton, Southampton, U.K., in 2013.

In 2001, he joined the Communication Systems section of the European Space Agency, Noordwijk, The Netherlands, where he conducted research in the field of spread-spectrum techniques for packet access in broadband satellite systems. From 2003 to 2010 he served at the European Patent Office, Rijswijk, The Netherlands, as Patent Examiner in the principal directorate of Telecommunications. In 2013, he joined the Satellite Oceanography section of the National Oceanography Centre, Southampton, where he currently works as a Research Scientist. His current research interests include remote sensing of the oceans, with special emphasis on techniques using signals of opportunity (GNSS-R).

Christine Gommenginger received the Diplome d'Etudes Approfondies degree in electromagnetics, telecommunications, and remote sensing from the University of Toulon, La Garde, France–University of Nice Sophia Antipolis, Nice, France, and the Ph.D. degree from the University of Southampton, Southampton, U.K., on microwave radar remote sensing of the ocean at low grazing angles.

She has worked at the National Oceanography Centre for over 20 years. Her research interests include active and passive microwave remote sensing of the ocean, understanding interactions of microwave signals with the ocean surface, remote sensing of ocean wind and waves, and developing new Earth Observation technologies and applications. Her work includes research in altimetry for sea state, along-track interferometric SAR for currents, global navigation satellite systems reflectometry for surface winds and sea state, SAR altimetry, salinity from space with SMOS, and wide-swath ocean altimetry.

Jason Hatton received the Ph.D. degree in Biology from the Universite Louis Pasteur Strasbourg, Strasbourg, France.

He is the Head of the Biology and Environmental Monitoring Unit in the Directorate of Human Spaceflight, European Space Agency, Paris, France. Since 2005, he has been responsible for the overall definition and coordination of biology and astrobiology science within the ESA ELIPS program, which are implemented on a variety of ground and flight research platforms, including the International Space Station. Furthermore, he is responsible for the overall coordination of the ESA ISS Experiments relevant to climate change, which includes the GEROS experiment. He also coordinated the joint ESA-NASA airborne observation campaign for the first ESA Automated Transfer Vehicle (ATV-1) re-entry in 2008. Prior to joining ESA he worked as a Researcher at the VA Medical Center/UCSF, San Francisco, CA, USA, from 2001 to 2005. He has performed research on immune cell early signal transduction under microgravity conditions, including a series of experiments using the ESA Biorack facility on Shuttle during the 1990s.

Per Høeg received the M.S. and Ph.D. degrees in geophysics and physics from the University of Copenhagen, Copenhagen, Denmark, in 1981 and 1987, respectively.

He has been a Researcher at the Danish Space Research Institute (1981–1986), the Max-Planck Institute for Aeronomy, Germany (1982–1985), and a Senior Researcher and the Head of Research at the Danish Meteorological Institute (1986–2004). His previous positions are external Associate Professor at the Niels Bohr Institute, University of Copenhagen (1994–2000), and a Professor at Aalborg University (2004–2009). Since 2009, he has been working as a Professor with the Technical University of Denmark (DTU), Kgs. Lyngby, Denmark, in satellite navigation, space technology, and atmosphere physics. His research interests include global navigation satellite systems (GNSS) satellite navigation, GNSS ocean reflections, ionosphere and atmosphere radio occultations, electromagnetic wave propagation, multipath phenomena, and turbulence.

Adrian Jäggi received the Ph.D. degree in astronomy from the University of Bern, Bern, Switzerland, in 2006.

Between 2007 and 2009, he was a Research Associate in the Astronomical Institute of the University of Bern (AIUB), and a Carl von Linde Junior Fellow in the Institute for Advanced Study, Technical University of Munich, Munich, Germany. In 2009, he became a Senior Research Scientist at AIUB and was responsible for research on precise orbit determination of low Earth satellites, gravity field recovery, and satellite laser ranging. Since 2012, he holds a Professorship of the University of Bern and is the Director of the AIUB. His main scientific interests include orbit and gravity field determination of artificial satellites orbiting the Earth, the Moon, and other planets. He is currently coordinating the H2020 project European Gravity Service for Improved Emergency Management.

Michael Kern received the Dipl.-Ing. degree in Geodesy from the Technical University of Karlsruhe (TH), Karlsruhe, Germany, in 1999, and the Ph.D. degree in geomatics engineering from the University of Calgary, Calgary, AB, Canada, in 2003.

He was a Research Assistant and Postdoctoral Fellow in the University of Calgary. He worked at the Graz University of Technology, Graz, Austria and received several post-doctoral European Space Agency fellowships. Since 2006, he is a Scientist in the Earth Surfaces and Interior Section at the European Space Agency, European Space Research and Technology Centre, Noordwijk, The Netherlands. He has been responsible for scientific research in conjunction with several ESA satellite missions and experiments including GOCE, Swarm, EE-7 candidate mission CoReH2O, MetOp-SG, and GEROS-ISS. His main scientific interests include gravity field research using satellite and airborne remote sensing data, cryosphere with a focus on snow, and global navigation satellite systems-reflectometry.

Tong Lee received the Ph.D. degree in physical oceanography from the University of Rhode Island, Kingston, RI, USA, in 1994.

From 1994 to 1996, he was a Postdoctoral Researcher at the Massachusetts Institute of Technology, Cambridge, MA, USA. Since 1996, he has been performing satellite oceanography and data assimilation research at NASA Jet Propulsion Laboratory, California Institute of Technology, Pasadena, CA, USA.

Zhijin Li received the Ph.D degree in atmospheric sciences from Lanzhou University, Lanzhou, China, in 1992.

He is currently a Scientist at the Jet Propulsion Laboratory, California Institute of Technology, Pasadena, CA, USA. His research interests include atmospheric and oceanic modeling, data assimilation, and numerical prediction. In the past decade, he has led the development of a hierarchy of data mapping and data assimilation methodologies for oceanic applications, and the development of several regional data assimilation and forecasting systems in support of oceanic field campaigns and operational applications. He has published more than 60 peer-reviewed papers.

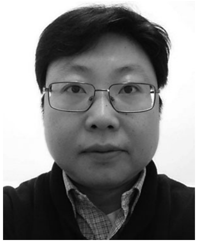

Hyuk Park was born in South Korea. He received the B.S. degree in mechanical engineering from the Korea Advanced Institute of Science and Technology, Daejeon, South Korea, in 2001, and the M.S. and Ph.D. degrees in information and mechatronics from the Gwangju Institute of Science and Technology, Gwangju, Korea, in 2003 and 2009, respectively.

In 2009, he joined the remote sensing group of the Polytechnic University of Catalonia (UPC), Barcelona, as a postdoctoral researcher. He was a grant holder of NRF funded by Korean government in 2011. From 2012, he has been working as a Researcher with Grant of Juan de la Cierva funded by Spanish Ministry of Science and Innovation. He is currently working with the passive remote sensing group in the UPC for satellite remote sensing for microwave radiometry and GNSS-R. His main research interests include the area of remote sensing, especially passive microwave remote sensing, including system design, modeling and simulation, and image processing.

Nazzareno Pierdicca (SM'xx) received the Laurea (Doctors) degree in electronic engineering (cum laude) from the University La Sapienza of Rome, Rome, Italy, in 1981.

From 1978 to 1982, he worked with the Italian Agency for Alternative Energy (ENEA). From 1982 to 1990, he was working with Telespazio, Rome, in the Remote Sensing Division. In November 1990, he joined the Department of Information Engineering, Electronics and Telecommunications, Sapienza University of Rome, Rome. He is currently a Full Professor and teaches remote sensing, antenna, and electromagnetic fields in the Faculty of Engineering, Sapienza University of Rome. His research interests include electromagnetic scattering and emission models for sea and bare soil surfaces and their inversion, microwave radiometry of the atmosphere, radar land applications, bistatic radar.

Prof. Pierdicca is a past Chairman of the GRSS Central Italy Chapter and member of the ESA GEROS-SAG.

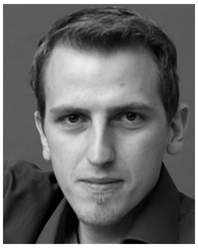

Gerhard Ressler received the Dipl.-Ing. degree in geomatics science from the Graz University of Technology, Graz, Austria, in 2011, the Graduate degree from the International Space University, Illkirch-Graffenstaden, France, in 2013 under an ESA fellowship.

He is currently with the Mission Science Division at ESA-European Space Research and Technology Centre, Noordwijk, The Netherlands, conducting performance analysis of existing and future GNSS-Reflectometry missions (GEROS-ISS) for scatterometry and altimetry applications. During his research at the German Geodetic Research Institute (DGFI-TUM) and a stay at the Planetary Geodynamics Laboratory at NASA Goddard Space Flight Center he focused on gravity-field analysis, primarily on regional spatio-temporal gravity-field modeling.

Antonio Rius received the Ph.D. degree in astrophysics from Barcelona University, Barcelona, Spain, in 1974.

From 1975 to 1985, he was a Member of the Technical Staff at NASA's Deep Space Communications Complex, Madrid, Spain, where he was responsible for the radio astronomical activities. Since 1986, he has been with the Spanish Consejo Superior de Investigaciones Científicas (CSIC), Barcelona. He is currently a CSIC Research Professor AH, working within the research group on Earth Observation at the Institut d'Estudis Espacials de Catalunya (ICE-CSIC/IEEC).

Josep Roselló received the engineering degree in telecommunications from the Politechnical University of Catalonia, Barcelona, Spain, in 1991.

He has been working at European Space Research and Technology Centre, Noordwijk, The Netherlands, for the European Space Agency, since 1993, in several areas such as data handling, on-board signal processing, GNSS transmitters and receivers, and SAR instruments. He is currently working at the Future Missions division of the Earth Observation Programme Directorate, with particular emphasis on GNSS scientific instruments and on the k-band data downlink.

Jan Saynisch received the diploma degree in physics from Potsdam University, Potsdam, Germany, in 2006, working on conceptual modeling of coupled climate phenomena, and the Ph.D. degree from the University of Bremen, Bremen, Germany, in 2009.

He worked at Alfred Wegener Institute, Bremerhaven, Germany, and studied ocean and Earth rotation interactions by numerical modeling and data assimilation. Since 2009, he works in the Earth System Modeling section, GFZ German Research Centre for Geosciences, Potsdam, where he combines numerical models and observations by adjoint and ensemble based data assimilation. His research interests include ocean dynamics, sea ice, tides, gravity field, Earth rotation, sea level, climate change, and magnetic field on global as on regional scales.

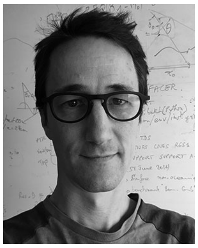

François Soulat received the Ph.D. degree in physics of remote sensing from the Catalan Polytechnic University, Barcelona, Spain, in 2004.

From 2001 to 2006, he was responsible of GNSS-R research projects in the Starlab company. He then spent almost two years in Mercator-Ocean, Toulouse, France, as the Manager of European projects dedicated to the Copernicus Marine Services. Since 2007, he has been working on SAR and InSAR radar altimetry at the Space Oceanography Division of Collecte Localisation Satellites. He is currently coordinating the phase B activities of the wide swath altimeter SWOT.

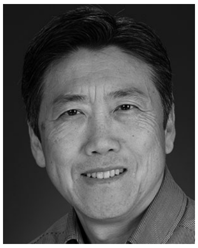

C. K. Shum is a Professor and Distinguished University Scholar in the Division of Geodetic Science, School of Earth Sciences, Ohio State University, Columbus, OH, USA.

He was a Lead Author in the 2007 IPCC Working Group I (The Physical Science Basis), Fourth Assessment Report (AR4) Chapter involving ocean climates and sea-level rise. He has published over 240 journal articles. He and his group focuses on research topics including the use of geodetic measurements and understanding of the geophysical causes of global sea level rise, under anthropogenic climate change.

Dr. Shum is a Fellow of the American Association for the Advancement of Science (AAAS) and a Fellow of the International Association of Geodesy. He received the Vening Meinesz Medal, awarded by the European Geosciences Union for distinguished research in Geodesy, and also many other awards.

Maximilian Semmling received the degree in physics from Leipzig University, Leipzig, Germany, and the Ph.D. degree from the Technical University of Berlin, Berlin, Germany, in 2007 and 2012, respectively.

Since 2008, he has been with the Department Geodesy of GFZ Potsdam, Germany. He is experienced in ground-based experiments for sea ice reflectometry in the Arctic (Disko Bay, Spitsbergen), airborne experiments for sea surface altimetry with a Zeppelin airship over Lake Constance and with the HALO (High Altitude LOng range) research aircraft over the Mediterranean Sea. In current studies, he concentrates on simulations of the GEROS-ISS phase altimetry and preparations for an airborne experiment to study GNSS ice sheets reflections over Antarctica. His research interests include the field of GNSS reflectometry and its application for remote sensing.

Ana Sousa received the first degree in geophysical sciences, branch Meteorology/Oceanography from Faculdade de Cincias da Universidade de Lisboa, Lisbon, Portugal, and the Master's degree in remote sensing from Faculdade de Cincias da Universidade do Porto, Porto, Portugal, in 2002 and 2007, respectively.

She is a Senior Engineer in the EO Ground Segment Systems Business Unit at DEIMOS Engenharia, Lisboa, Portugal. She has a large experience in data processing and end-to-end instrument simulation. She is currently the Technical Manager of the GEROS and GARCA projects, both regarding GNSS-R activities and had also been involved in the Sentinel 3 Optical Ground Processor Level 1 Prototype regarding software development activities of the data processor for SLSTR instrument. She was also responsible for the development of an automatic geometry correction processor in the scope of GERSI (physical model for analyzing the geometric errors of remote sensing imagery) project.

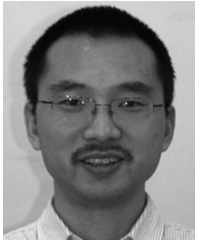

Jiping Xie received the Ph.D. degree in Nature Science, Geophysical fluid dynamics from the Institute of Atmospheric Physics, Chinese Academy of Sciences, Beijing, China, in 2008.

He has 10 years of experience in ocean modeling and data assimilation. He is currently a Researcher at Nansen Environmental and Remote Sensing Center, Bergen, Norway, in charge of producing the Arctic reanalysis in the Copernicus Arctic MFC with the TOPAZ system.

Cinzia Zuffada received a Doctorate in electronic engineering degree from the University of Pavia, Pavia, Italy.

She was an Assistant Professor in Electromagnetic Fields Theory in the University of Pavia. She joined the Jet Propulsion Laboratory (JPL), Pasadena, CA, USA, in 1992, and is currently the Associate Chief Scientist. Additionally, she oversees a number of programs supporting collaborations between JPL and the academic community. Prior to this position, she was the Manager of the Earth Remote Sensing Section of the JPL Science division. As a Researcher, she pioneered the global navigation satellite system reflectometry technique for ocean remote sensing and contributed to electromagnetic scattering and radiation research.